In Vivo Thermodynamic Analysis of Glycolysis in *Clostridium thermocellum* and *Thermoanaerobacterium saccharolyticum* Using ¹³C and ²H Tracers

Tyler B. Jacobson,[a,b] Travis K. Korosh,[a,b] David M. Stevenson,[a,b] Charles Foster,[a,c] Costas Maranas,[a,c] Daniel G. Olson,[a,d] Lee R. Lynd,[a,d] Daniel Amador-Noguez[a,b]

[a]Center for Bioenergy Innovation, Oak Ridge National Laboratory, Oak Ridge, Tennessee, USA
[b]Department of Bacteriology, University of Wisconsin–Madison, Madison, Wisconsin, USA
[c]Department of Chemical Engineering, The Pennsylvania State University, University Park, Pennsylvania, USA
[d]Thayer School of Engineering, Dartmouth College, Hanover, New Hampshire, USA

ABSTRACT *Clostridium thermocellum* and *Thermoanaerobacterium saccharolyticum* are thermophilic anaerobic bacteria with complementary metabolic capabilities that utilize distinct glycolytic pathways for the conversion of cellulosic sugars to biofuels. We integrated quantitative metabolomics with ²H and ¹³C metabolic flux analysis to investigate the *in vivo* reversibility and thermodynamics of the central metabolic networks of these two microbes. We found that the glycolytic pathway in *C. thermocellum* operates remarkably close to thermodynamic equilibrium, with an overall drop in Gibbs free energy 5-fold lower than that of *T. saccharolyticum* or anaerobically grown *Escherichia coli*. The limited thermodynamic driving force of glycolysis in *C. thermocellum* could be attributed in large part to the small free energy of the phosphofructokinase reaction producing fructose bisphosphate. The ethanol fermentation pathway was also substantially more reversible in *C. thermocellum* than in *T. saccharolyticum*. These observations help explain the comparatively low ethanol titers of *C. thermocellum* and suggest engineering interventions that can be used to increase its ethanol productivity and glycolytic rate. In addition to thermodynamic analysis, we used our isotope tracer data to reconstruct the *T. saccharolyticum* central metabolic network, revealing exclusive use of the Embden-Meyerhof-Parnas (EMP) pathway for glycolysis, a bifurcated tricarboxylic acid (TCA) cycle, and a sedoheptulose bisphosphate bypass active within the pentose phosphate pathway.

IMPORTANCE Thermodynamics constitutes a key determinant of flux and enzyme efficiency in metabolic networks. Here, we provide new insights into the divergent thermodynamics of the glycolytic pathways of *C. thermocellum* and *T. saccharolyticum*, two industrially relevant thermophilic bacteria whose metabolism still is not well understood. We report that while the glycolytic pathway in *T. saccharolyticum* is as thermodynamically favorable as that found in model organisms, such as *E. coli* or *Saccharomyces cerevisiae*, the glycolytic pathway of *C. thermocellum* operates near equilibrium. The use of a near-equilibrium glycolytic pathway, with potentially increased ATP yield, by this cellulolytic microbe may represent an evolutionary adaptation to growth on cellulose, but it has the drawback of being highly susceptible to product feedback inhibition. The results of this study will facilitate future engineering of high-performance strains capable of transforming cellulosic biomass to biofuels at high yields and titers.

_T_hermoanaerobacterium saccharolyticum and _Clostridium thermocellum_ are thermophilic, anaerobic bacteria with complementary metabolic capabilities being developed for industrial-scale production of biofuels, such as ethanol, from lignocellulosic biomass (1–3). _C. thermocellum_ readily solubilizes lignocellulosic biomass and ferments cellulose-derived sugars, including oligomers, to ethanol, acetate, lactate, formate, and H_2. However, _C. thermocellum_ is incapable of utilizing the hemicellulose fraction of biomass (containing xylose, arabinose, mannose, and galactose) (4, 5). Metabolic engineering efforts have increased the native ethanol yields and titers of _C. thermocellum_, but the best strains, with a titer of ~25 g/liter and 75% theoretical yield, do not yet match the productivity of noncellulolytic ethanologens such as _Saccharomyces cerevisiae_ and _Zymomonas mobilis_ (6–9). In contrast, _T. saccharolyticum_ cannot solubilize lignocellulosic biomass or cellulose but readily ferments hemicellulose-derived sugars, including oligomers, to ethanol, acetate, lactate, and H_2 (4, 10). _T. saccharolyticum_ has been engineered to produce ethanol at greater than 90% theoretical yields and at titers of up to 70 g/liter (3, 10). These two thermophilic bacteria have been used in cocultures that seek to combine the cellulolytic capability of _C. thermocellum_ with the higher ethanol productivity and hemicellulose-consuming capability of _T. saccharolyticum_ (11). Several previous studies have directly compared the fermentation capabilities of _C. thermocellum_ and _T. saccharolyticum_, and _T. saccharolyticum_ has been used frequently as a source of genes to engineer enhanced ethanol productivity in _C. thermocellum_ (12–19).

In addition to the differences outlined above, _T. saccharolyticum_ and _C. thermocellum_ possess distinct glycolytic pathways. While genome annotation suggests that _T. saccharolyticum_ uses the canonical Embden-Meyerhof-Parnas (EMP) pathway, the glycolytic pathway in _C. thermocellum_ has been shown to possess several unique characteristics (18, 20–23) (Fig. 1). Most notably, the conversion of fructose-6-phosphate (F6P) to fructose-1,6-bisphosphate (FBP), catalyzed by phosphofructokinase (Pfk), is coupled to pyrophosphate (PP_i) rather than ATP hydrolysis (20, 24, 25). In addition, glucokinase (Glk; Glc + NTP→G6P) utilizes GTP instead of ATP as the high-energy phosphate donor, and phosphoglycerate kinase (Pgk; BPG + NDP → 3PG + NTP) is capable of producing both ATP and GTP (20, 26). Finally, _C. thermocellum_ lacks a pyruvate (Pyr) kinase (Pyk; PEP + ADP→Pyr + ATP) and instead converts phosphoenolpyruvate (PEP) to Pyr via one of two routes: (i) pyruvate phosphate dikinase (Ppdk; PEP + AMP + PP_i→Pyr + ATP + P_i) and (ii) the malate shunt, which converts PEP to Pyr via three steps, phosphoenolpyruvate carboxykinase (Pepck; PEP + GDP + CO_2→OAA + GTP), malate dehydrogenase (Mdh; OAA + NADH→Mal + NAD^+), and malic enzyme (ME; Mal + $NADP^+$→Pyr + CO_2 + NADPH + H^+) (18, 20, 21, 26) (Fig. 1). These unique aspects of glycolysis in _C. thermocellum_, particularly the use of PP_i-Pfk and Ppdk, may result in greater energy yield (ATP or GTP) per glucose but also can be expected to significantly impact the thermodynamic driving force of individual reactions and of the overall pathway.

Recently developed experimental approaches for estimating _in vivo_ Gibbs free energies (ΔG) of metabolic reactions have been applied to investigate the thermodynamics of glycolytic pathways in a few model organisms and biofuel producers (27–29). The estimation of ΔG by these approaches relies on the fundamental relation of $\Delta G = -RT \ln(J^+/J^-)$ (30) and the determination of forward (J^+) to backward (J^-) flux ratios (J^+/J^-) from isotope tracer experiments (R is the gas constant and T is the temperature in kelvin) (27, 29). These studies, together with theoretical and computational advances, have provided new insights on the connection between pathway thermodynamics, flux, and enzyme efficiency (31–34).

Here, we integrated quantitative metabolomics with ^2H and ^{13}C metabolic flux analysis to investigate the _in vivo_ reversibility and thermodynamics of the glycolytic pathways and central metabolic networks of _T. saccharolyticum_ and _C. thermocellum_. We show that glycolysis in _C. thermocellum_ is highly reversible at every step of the pathway and operates close to thermodynamic equilibrium. In comparison, the glycolytic pathway in _T. saccharolyticum_ is highly thermodynamically favorable, comparable

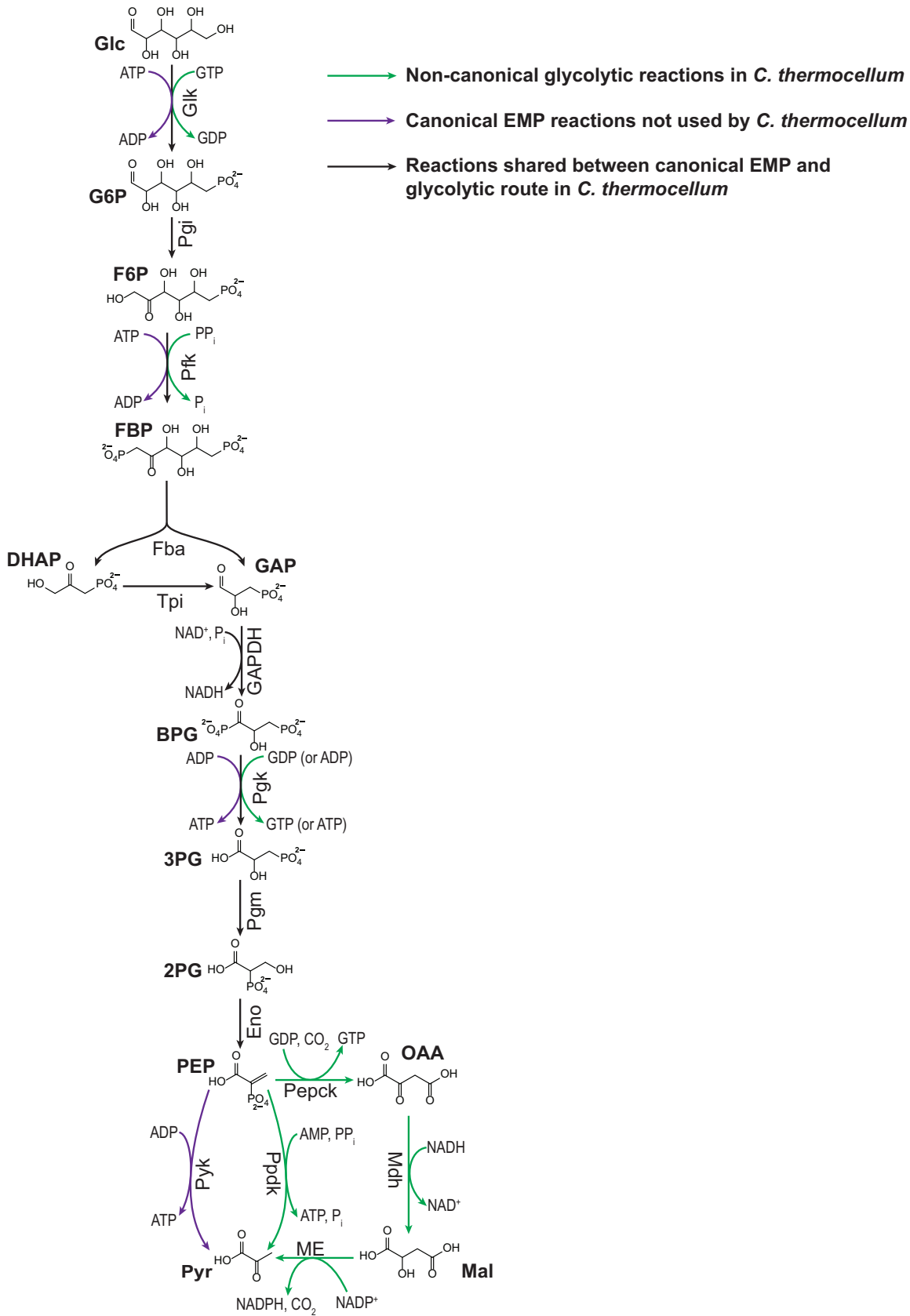**FIG 1** Glycolytic pathway of *C. thermocellum*. *C. thermocellum* uses a glycolytic pathway that differs from the canonical EMP pathway. Black arrows represent reactions that are common between EMP glycolysis and *C. thermocellum* glycolysis. Green arrows represent reactions unique to glycolysis in *C. thermocellum*. Purple arrows represent EMP glycolytic reactions not present in *C. thermocellum*.

(Continued on next page)

to that of anaerobically grown *Escherichia coli*. We also found that the ethanol fermentation pathway of *C. thermocellum* was substantially more reversible than that of *T. saccharolyticum*. Besides revealing differences in pathway reversibility, our analyses also represent the first experimental isotope-based reconstruction of the *T. saccharolyticum* central metabolic network. We found that this bacterium metabolizes glucose exclusively via the EMP pathway, while the Entner-Doudoroff (ED) pathway and the oxidative pentose phosphate pathway (oxPPP) are inactive. Our analyses also revealed a bifurcated tricarboxylic acid (TCA) cycle and a sedoheptulose bisphosphate bypass within the pentose phosphate pathway (PPP). Finally, we present evidence supporting the activity of several currently unannotated amino acid biosynthetic pathways in *T. saccharolyticum*.

RESULTS

Reconstruction of the *T. saccharolyticum* central metabolic network. The application of ^{2}H and ^{13}C metabolic flux analysis to measure *in vivo* reversibility and thermodynamics of metabolic reactions requires prior knowledge of the underlying metabolic network topology. Recent studies have used isotope tracers, metabolic flux analysis (MFA), proteomics, or biochemical assays to elucidate the central metabolic network of *C. thermocellum* (14, 18, 20, 21, 24, 26, 35–38). However, although the genome sequence of *T. saccharolyticum* is available and systems-level approaches were used to characterize its physiology (22, 23, 39, 40), an isotope-based reconstruction of its metabolic network is currently lacking. To address this knowledge gap, we performed parallel steady-state labeling experiments by growing cells in [1-^{13}C$_1$]glucose, [6-^{13}C$_1$]glucose, [1,2-^{13}C$_2$]glucose, or a 50:50 mixture of [U-^{13}C$_6$]glucose and unlabeled glucose. Using these ^{13}C labeling data, we first carried out a manual evaluation and reconstruction of the *T. saccharolyticum* central metabolic network. In a subsequent section (i.e., "^{2}H and ^{13}C metabolic flux analysis," below), we present a quantitative MFA that corroborates the metabolic network reconstruction presented in this section.

(i) Glucose catabolism. The Embden-Meyerhof-Parnas (EMP) and the Entner-Doudoroff (ED) pathways are the two most common glycolytic pathways found in microbial species, although several other variants have been described (20, 31, 41–43). The EMP and ED pathways share a common set of reactions that metabolize glyceraldehyde-3-phosphate (GAP) into pyruvate (Pyr) (i.e., lower glycolysis), but they differ in their initial steps (Fig. 2A and B). In the ED pathway, the intermediate 2-keto-3-deoxy-6-phosphogluconate (KDPG) is cleaved into Pyr (first three carbons) and GAP (last three carbons). Therefore, unlike in the EMP pathway (in which two GAP molecules are produced from glucose), the first three carbons of glucose bypass lower glycolysis in the ED pathway. Additionally, carbons 1, 2, and 3 of glucose catabolized via the ED pathway become the carboxyl, carbonyl, and methyl carbons, respectively, of Pyr, which is the reverse order of that obtained via the EMP pathway (Fig. 2C). *T. saccharolyticum* has genes encoding all of the enzymes in the EMP pathway, but its genome annotation does not support a complete ED pathway. *T. saccharolyticum* does not have sequences associated with the ED enzymes phosphogluconolactonase (Pgl; gluconolactone phosphate [GLP] + H$_2$O→6-phosphogluconate [6PG]) or phosphogluconate dehydratase (Edd; 6PG→KDPG), although it does have genes annotated as glucose-6-phosphate dehydrogenase [G6pdh; G6P + NAD(P)$^+$→GLP + NAD(P)H, *Tsac_1610*] and ED pathway aldolase (Eda; KDPG→GAP + Pyr; *Tsac_0268*) (22, 23).

FIG 1 Legend (Continued)

Abbreviations: 2PG, 2-phosphoglycerate; 3PG, 3-phosphoglycerate; BPG, 1,3-bisphosphoglycerate; DHAP, dihydroxyacetone phosphate; EMP, Embden-Meyerhof-Parnas pathway; Eno, phosphopyruvate hydratase; F6P, fructose-6-phosphate; Fba, fructose-1,6-bisphosphate aldolase; FBP, fructose-1,6-bisphosphate; G6P, glucose-6-phosphate; GAP, glyceraldehyde-3-phosphate; GAPDH, glyceraldehyde-3-phosphate dehydrogenase; Glc, glucose; Glk, glucokinase; Mal, malate; Mdh, malate dehydrogenase; ME, malic enzyme; OAA, oxaloacetate; PEP, phosphoenolpyruvate; Pepck, phosphoenolpyruvate carboxykinase; Pfk, phosphofructokinase; Pgi, phosphoglucose isomerase; Pgk, phosphoglycerate kinase; Pgl, phosphogluconolactonase; Pgm, phosphoglycerate mutase; Ppdk, pyruvate phosphate dikinase; PPi, pyrophosphate; Pyk, pyruvate kinase; Pyr, pyruvate; Tpi, triose-phosphate isomerase.
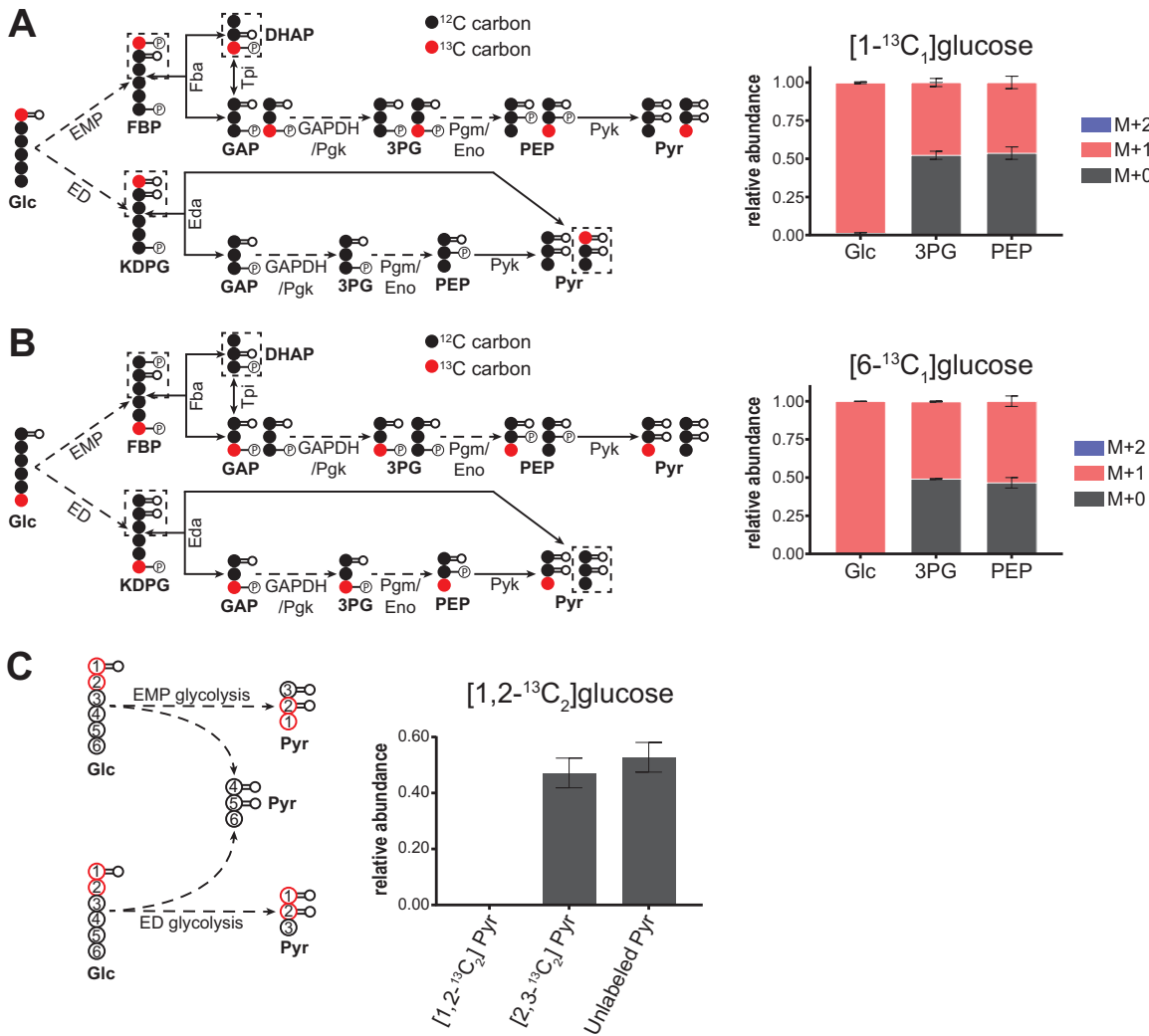
FIG 2 EMP is the primary glycolytic route in *T. saccharolyticum*. (A and B) Labeling of lower glycolytic intermediates 3PG and PEP when *T. saccharolyticum* was fed [1-$^{13}C_1$]glucose or [6-$^{13}C_1$]glucose. In both cases, 3PG and PEP were ~50% M + 0 and ~50% M + 1, which was consistent with their production exclusively via EMP glycolysis. The diagrams on the left depict predicted metabolite labeling via EMP or ED glycolysis. Solid arrows represent a single reaction; dashed arrows represent multiple reaction steps. ^{13}C-labeled carbons are colored red; ^{12}C-carbons are colored black. Data are averages from 2 independent biological replicates. Error bars show ± standard deviations (SD). (C) As shown in the diagram, glucose catabolism by the EMP and ED pathways results in different ordering of carbons in the pyruvate formed from the first three carbons of glucose. When *T. saccharolyticum* was fed [1,2-$^{13}C_2$]glucose, essentially all pyruvate was either unlabeled or labeled at the second (i.e., carbonyl group) and third (i.e., methyl group) carbons (i.e., [2,3-$^{13}C_2$]Pyr), consistent with exclusive use of the EMP pathway. If the ED pathway were active, pyruvate would have been labeled at the first and second carbons (i.e., [1,2-$^{13}C_2$]Pyr), but we detected <0.1% of this form of pyruvate. ^{13}C-labeled carbons are represented as open circles with a red outline; ^{12}C-labeled carbons are represented as open circles with a black outline. The number in each circle corresponds to their original position in glucose. Data are averages from 2 independent biological replicates. Error bars show ±SD. Abbreviations: ED, Entner-Doudoroff pathway; Eda, KDPG aldolase; KDPG, 2-keto-3-dehydro-6-phosphogluconate.

When *T. saccharolyticum* was grown on [1-$^{13}C_1$]- or [6-$^{13}C_1$]glucose, the glycolytic intermediates 3-phosphoglycerate (3PG) and phosphoenolpyruvate (PEP) both were ~50% M + 0 (i.e., unlabeled; all carbons are ^{12}C, where M represents the unlabeled parent mass) and ~50% M + 1 (i.e., containing one ^{13}C carbon), which was consistent with their production via EMP glycolysis (Fig. 2A and B). If the ED pathway was the exclusive glycolytic pathway, 3PG and PEP would have been 100% M + 0 in [1-$^{13}C_1$]glucose or 100% M + 1 in [6-$^{13}C_1$]glucose [27]. If both the EMP and ED pathways were active, labeling of 3PG and PEP would have been <50% M + 1 in [1-$^{13}C_1$]glucose and >50% M + 1 in [6-$^{13}C_1$]glucose. For example, equal utilization of the EMP and ED pathways would result in 25% M + 1 3PG and PEP in [1-$^{13}C_1$]glucose and 75% M + 1 3PG and PEP in [6-$^{13}C_1$]glucose. As additional support for the absence of ED pathway

activity, when *T. saccharolyticum* was fed [1,2-$^{13}C_2$]glucose, Pyr was labeled only at the second and third carbon (i.e., [2,3-$^{13}C_2$]Pyr), consistent with its production solely via the EMP pathway (Fig. 2C). We did not detect Pyr labeled at the first and second carbons (i.e., [1,2-$^{13}C_2$]Pyr), which would have been indicative of ED pathway activity (27).

Finally, as shown in Table S1 in the supplemental material, high intracellular levels of the EMP intermediates FBP and dihydroxyactone phosphate (DHAP), which were comparable to those in anaerobic *E. coli*, a known EMP-utilizing organism, together with nondetectable levels of the ED pathway intermediates 6PG and KDPG, which are present in the ED pathway, utilizing organisms such as *Z. mobilis*, was consistent with the existence of an active EMP pathway and an inactive ED pathway in *T. saccharolyticum* (27, 44).

(ii) Pentose phosphate pathway and sedoheptulose bisphosphate bypass. The oxPPP converts glucose-6-phosphate (G6P) to 6PG via the G6pdh and Pgl reactions, which are shared with the ED pathway. 6PG then is decarboxylated by 6-phosphogluconate dehydrogenase [6pgd; 6PG + NAD(P)$^+ \rightarrow$ Ru5P + CO_2 + NAD(P)H] to form ribulose-5-phosphate (Ru5P), losing what was originally the first carbon of glucose as CO_2 (Fig. 3). *T. saccharolyticum* has annotated genes for *g6pdh* (*Tsac_1610*) and *6pgd* (*Tsac_0154*) genes, but there are no annotated *pgl* sequences (22, 23, 45). Our labeling data indicated that the oxPPP was essentially inactive in *T. saccharolyticum*, since less than 1% of Ru5P was present as M + 1 when cells were grown on [1,2-$^{13}C_2$]glucose (Fig. 3A). Nondetectable levels of the intermediate 6PG were consistent with the lack of an active oxPPP (46, 47).

The nonoxidative production of pentose phosphates typically proceeds via a transketolase reaction (Tkt1; F6P + GAP$\rightarrow$E4P + Xu5P), a transaldolase reaction (Tal; E4P + F6P$\rightarrow$S7P + GAP), and a second transketolase reaction (Tkt2; S7P + GAP$\rightarrow$R5P + Xu5P). Additionally, ribose phosphate epimerase (Rpe; Xu5P$\rightarrow$Ru5P) and ribose phosphate isomerase (Rpi; Ru5P$\rightarrow$R5P) interconvert Xu5P, Ru5P, and R5P. In *T. saccharolyticum*, R5P and Ru5P were predominantly M + 2 and M + 4 labeled in [1,2-$^{13}C_2$]glucose and M + 1 and M + 2 labeled in [1-$^{13}C_1$]glucose (Fig. 3B and C), which was consistent with their production via the nonoxidative PPP reactions listed above.

Interestingly, we found the production of a large fraction (30 to 40%) of M + 0 S7P in both [1,2-$^{13}C_2$]- and [1-$^{13}C_1$]glucose that could not be explained by canonical nonoxidative PPP reactions (Fig. 3A and B). For example, taking into account the observed labeling patterns of PPP intermediates during growth in [1,2-$^{13}C_2$]- or [1-$^{13}C_1$]glucose, no more than 10% M + 0 S7P should be present under either condition if Tal and Tkt1 were the only reactions producing S7P. Therefore, the large unexpected fraction of M + 0 S7P suggested that another route for S7P production should be present. Specifically, these data suggested that *T. saccharolyticum* possesses a sedoheptulose bisphosphate (SBP) bypass comprising an SBP aldolase (Sba; DHAP + E4P$\rightarrow$SBP) and an SBP phosphatase (SBPase; SBP + $P_i \rightarrow$S7P + pyrophosphate [PP_i]) (24, 26). While there are no genes associated with SBPase activity in *T. saccharolyticum*, several genes (i.e., *Tsac_0260*, *Tsac_0328*, and *Tsac_2313*) are annotated as both Fbas and Sbas (22, 23), and one or more of these could be responsible for the observed Sba activity (48).

This SBP bypass can explain the production of unlabeled S7P from unlabeled DHAP and E4P during growth on [1-$^{13}C_1$]- and [1,2-$^{13}C_2$]glucose. Similarly, during [6-$^{13}C_1$]glucose labeling, the large fraction of M + 2 S7P (~32.5%) was also indicative of SBP bypass activity (Fig. 3C). Alternative PPP routes, such as phosphoketolase, formaldehyde transketolase, and the reverse ribulose monophosphate (RuMP) pathway, cannot explain the observed PPP labeling patterns (Fig. S1).

(iii) TCA cycle. Several TCA cycle enzymes remain unannotated in the *T. saccharolyticum* genome, including citrate synthase and malate dehydrogenase. Our ^{13}C tracer data indicated that the TCA cycle in *T. saccharolyticum* functions as a branched pathway to produce essential biosynthetic precursors: α-ketoglutarate (AKG) was produced oxidatively despite the lack of an annotated citrate synthase, while oxaloacetate (OAA),
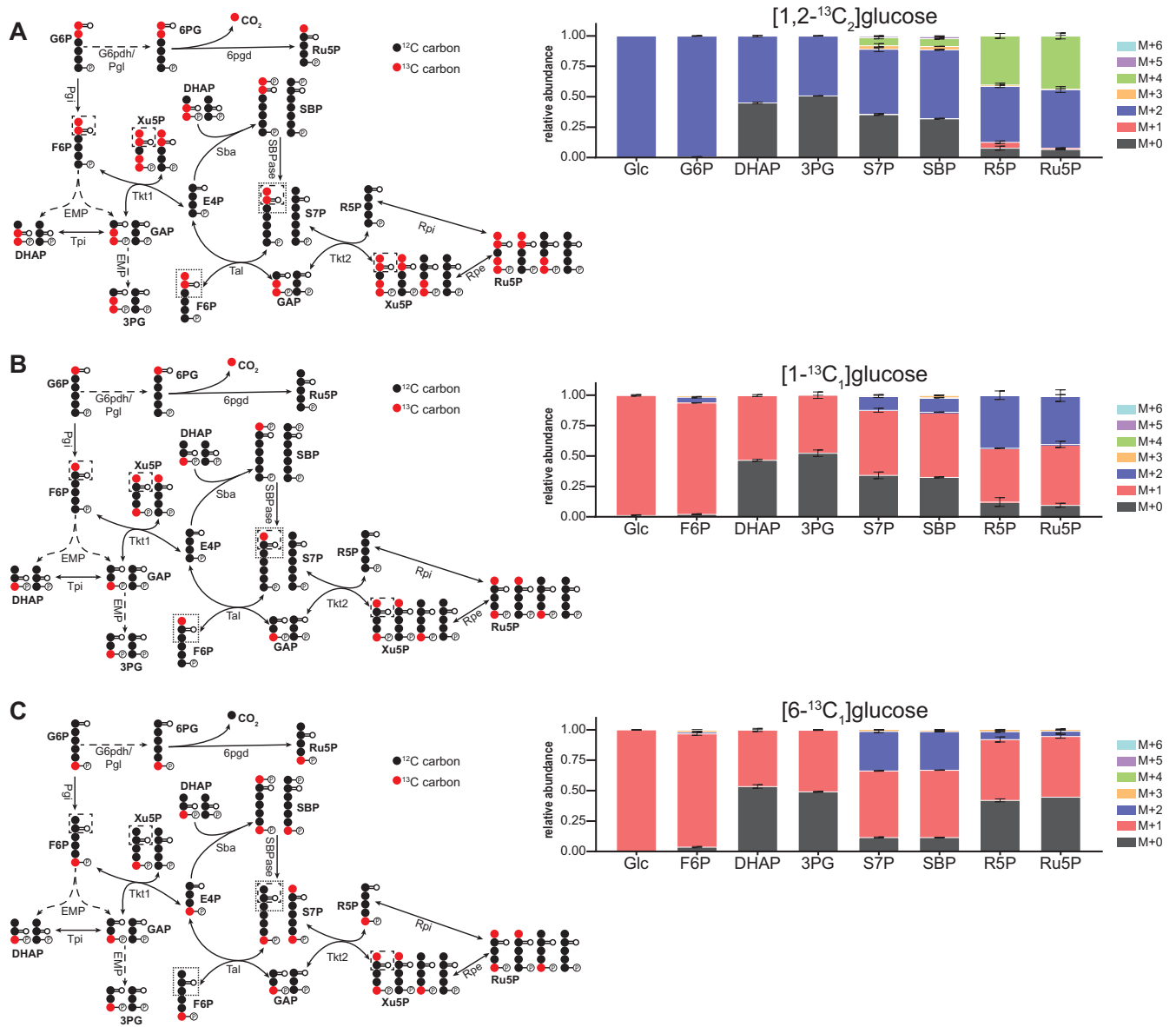
FIG 3 *T. saccharolyticum* has two nonoxidative routes for pentose phosphate production. Labeling of glycolytic and PPP intermediates when *T. saccharolyticum* was fed [1,2-$^{13}C_2$]glucose (A), [1-$^{13}C_1$]glucose (B), or [6-$^{13}C_1$]glucose (C). As described in the text, labeling patterns indicated that the oxidative branch of the PPP was essentially inactive and suggested the presence of a sedoheptulose bisphosphate bypass, comprising SBP aldolase (Sba) and SBP phosphatase (SBPase). The diagrams on the left show predicted metabolite labeling with the specified isotope tracer. Solid arrows represent a single reaction; dashed arrows represent multiple reaction steps. Dotted boxes indicate carbons transferred during transaldolase and transketolase reactions. ^{13}C-labeled carbons are colored red; ^{12}C-labeled carbons are colored black. Data are averages from 2 or 3 independent biological replicates. Error bars show ±SD. Abbreviations: 6PG, 6-phosphogluconate; 6pgd, 6-phosphogluconate dehydrogenase; E4P, erythrose-4-phosphate; G6pdh, glucose-6-phosphate dehydrogenase; R5P, ribose-5-phosphate; Rpe, ribose phosphate epimerase; Rpi, ribose phosphate isomerase; Ru5P, ribulose-5-phosphate; S7P, sedoheptulose-7-phosphate; Sba, sedoheptulose-1,7-bisphosphate aldolase; SBP, sedoheptulose-1,7-bisphosphate; SBPase, sedoheptulose-1,7-bisphosphate phosphatase; Tal, transaldolase; Tkt1, transketolase reaction 1; Tkt2, transketolase reaction 2; Xu5P, xylulose-5-phosphate.

malate (Mal), and succinate all were produced reductively. During growth in [6-$^{13}C_1$]glucose, α-ketoglutarate (AKG) labeling patterns were consistent with its production from oxaloacetate and acetyl-coenzyme A (AcCoA) via citrate and isocitrate (Fig. 4). However, although AKG was ~23% M + 2, succinate was <0.6% M + 2, indicating negligible oxidative succinate production from AKG via an AKG dehydrogenase. Although several genes in *T. saccharolyticum* are annotated as a 2-oxoacid/AKG:ferredoxin dehydrogenase, there is no gene specifically annotated as an AKG dehydrogenase (22, 23, 45). Instead, labeling patterns in succinate, Mal, and aspartate (here being
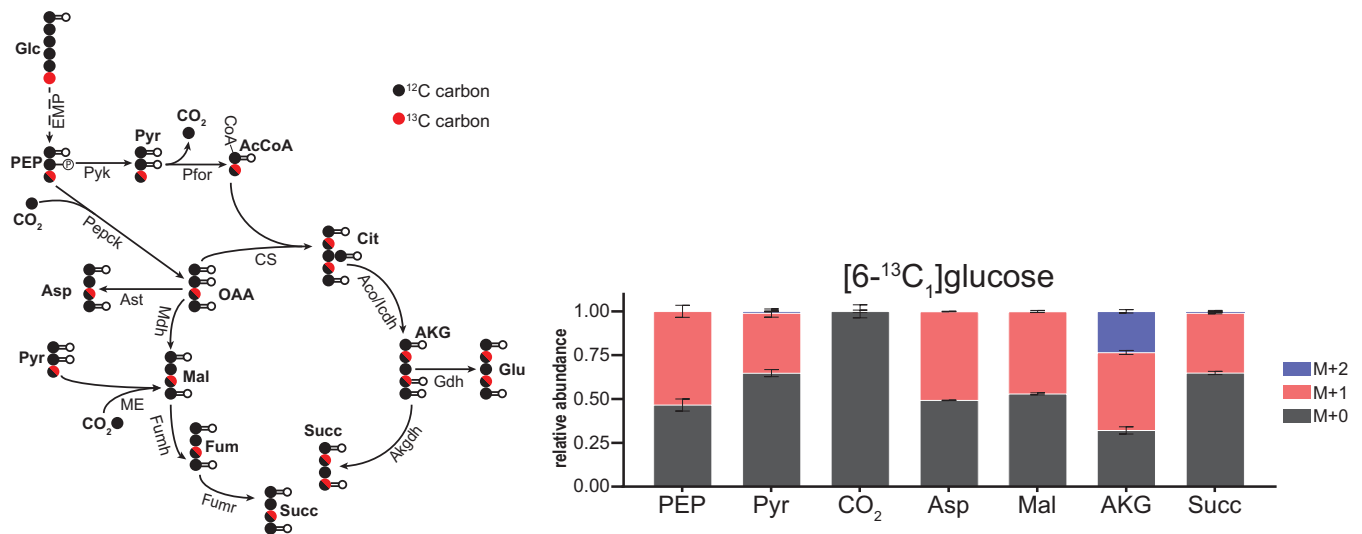
FIG 4 *T. saccharolyticum* TCA cycle is bifurcated. Labeling of lower glycolytic and TCA cycle intermediates when *T. saccharolyticum* was fed [6-^{13}C$_1$]-glucose. α-Ketoglutarate (AKG) labeling patterns were consistent with its production from oxaloacetate and acetyl-CoA via an oxidative TCA. The presence of M + 2 α-ketoglutarate but near absence of M + 2 succinate indicated that the TCA cycle was bifurcated. Labeling patterns in succinate, malate, and aspartate (used as a surrogate for oxaloacetate) were consistent with their production via a reductive TCA. Experiments with [1-^{13}C$_1$] and [1,2-^{13}C$_2$]glucose confirmed these findings (Fig. S2). In addition to its production via Fumh, fumarate can be produced by deamination of aspartate, which occurs in biosynthetic pathways such as purine biosynthesis. This route of fumarate production would result in the same labeling patterns as its production from oxaloacetate via Mdh and Fumh. The increased proportion of M + 0 pyruvate, succinate, α-ketoglutarate, and malate was due to extracellular pools of these metabolites that do not become labeled. CO$_2$ labeling was inferred from the mass isotopomer distributions (MIDs) of citrulline and ornithine, as described in Materials and Methods. The diagram on the left shows predicted metabolite labeling with [6-^{13}C$_1$]glucose. Pyruvate formate lyase (Pfl) was omitted from the figure but serves the same role as Pfor. Solid arrows represent a single reaction; dashed arrows represent multiple reaction steps. ^{13}C-labeled carbons are colored red; ^{12}C-labeled carbons are colored black. Data are averages from 2 independent biological replicates. Error bars show ±SD. Abbreviations: AcCoA, acetyl-coenzyme A; Aco, aconitase; AKG, α-ketoglutarate; Akgdh, α-ketoglutarate dehydrogenase; Asp, aspartate; Ast, aspartate transaminase; Cit, citrate; CoA, coenzyme A; CS, citrate synthase; Fum, fumarate; Fumh, fumarate hydratase; Fumr, fumarate reductase; Gdh, glutamate dehydrogenase; Glu, glutamate; Icdh, isocitrate dehydrogenase; Pfor, pyruvate ferredoxin oxidoreductase; Succ, succinate.

used as a surrogate for OAA) were consistent with their production via a reductive TCA (Fig. 4). As detailed in Fig. S1, [1-^{13}C$_1$]- and [1,2-^{13}C$_2$]glucose labeling confirmed the production of succinate, Mal, and aspartate via the reductive TCA.

(iv) TCA cycle anaplerosis. Anaplerotic reactions transform PEP and Pyr into TCA cycle intermediates, such as OAA and Mal. According to its genome annotation, *T. saccharolyticum* has a malic enzyme (ME; Mal + NADP$^+$→Pyr + CO$_2$ + NADPH + H$^+$; *Tsac_0488*, *Tsac_0975*) and a phosphoenolpyruvate carboxykinase (Pepck; OAA + ATP→PEP + CO$_2$ + ADP; *Tsac_2170*), which is typically considered a gluconeogenic enzyme (22, 23, 45). When *T. saccharolyticum* was fed an equimolar mixture of [U-^{13}C$_6$]glucose and unlabeled glucose, some M + 2 pyruvate (14.7%) was produced due to reversibility of pyruvate ferredoxin oxidoreductase (Pfor; Pyr + CoA + Fd$_{ox}$ → AcCoA + CO$_2$ + Fd$_{red}$) or pyruvate formate lyase (Pfl; Pyr + CoA → AcCoA + Form) (M + 1 pyruvate is produced in a similar fashion). Thus, the presence of M + 2 aspartate (surrogate for OAA) and M + 2 Mal indicated production of these two metabolites from pyruvate, likely via ME (Fig. 5A). However, the M + 2 fraction in aspartate (9.1%) and Mal (7.7%) was smaller than that of Pyr ($P < 0.05$ for both pairwise comparisons), which suggested that PEP, with an M + 2 fraction (3.9%) smaller than that of Pyr ($P < 0.05$), also contributed to the production of these two metabolites via Pepck or via an unannotated PEP carboxylase.

(v) Amino acid synthesis and one-carbon metabolism. Our ^{13}C-tracer data confirmed that aspartate, asparagine, and threonine were produced via canonical routes starting from oxaloacetate (Fig. S2A). Similarly, our data supported production of glutamate, glutamine, ornithine, citrulline, and proline via canonical pathways starting with AKG (Fig. S2B). The amino acids valine and leucine were also produced via canonical branched-chain amino acid synthesis pathways from the intermediate ketoisovalerate (Fig. S2C). Finally, ^{13}C-labeling patterns in the aromatic amino acids
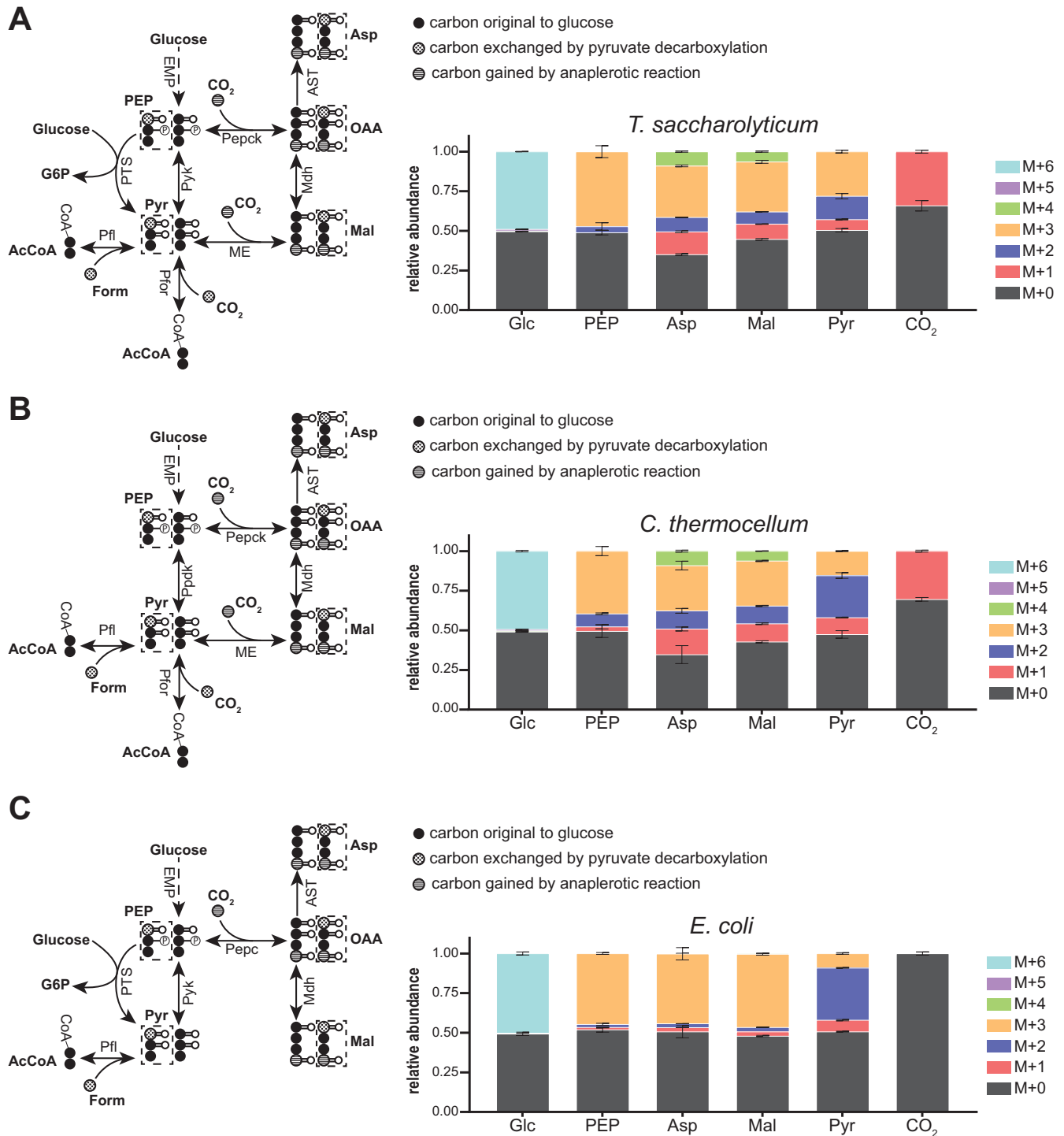
FIG 5 Reversibility of PEP-to-Pyr conversion. Steady-state labeling patterns of lower glycolytic intermediates in *T. saccharolyticum* (A), *C. thermocellum* (B), and *E. coli* (C) during anaerobic growth on an equimolar mixture of [U^{13}C$_6$]glucose and unlabeled glucose. In all three bacteria, forward glycolytic flux produced M + 0 or M + 3 PEP and pyruvate. Carboxylation of PEP or pyruvate to form oxaloacetate (OAA) or malate (Mal) resulted in M + 4 OAA/Mal (from M + 3 pyruvate and labeled CO$_2$) or M + 1 OAA/Mal (from M + 0 pyruvate and labeled CO$_2$). Reversible decarboxylation of pyruvate by Pfor or Pfl resulted in the production of M + 1 pyruvate (from M + 0 pyruvate and labeled CO$_2$/formate) and M + 2 pyruvate (from M + 3 pyruvate and unlabeled CO$_2$/formate). Once formed, M + 1 or M + 2 pyruvate propagated back to PEP. The higher proportion of M + 1 or M + 2 PEP in *C. thermocellum* indicated that the conversion of PEP to pyruvate was most reversible in this bacterium. *T. saccharolyticum* displayed only moderate reversibility of this conversion, while *E. coli* displayed almost no reversibility. CO$_2$ labeling was inferred from the MIDs of citrulline and ornithine, as described in Materials and Methods. The pyruvate MID was inferred from the MID of valine. The diagrams on the left display the reactions surrounding the PEP/pyruvate node of each bacteria. Black circles represent carbons that originate in glucose; dotted circles represent carbons that can be exchanged by the pyruvate decarboxylating reactions (Pfor or Pfl); striped circles represent carbons that are gained during the anaplerotic reactions (ME, Pepck, and Pepc). Solid arrows represent a single reaction; dashed arrows represent multiple reaction steps. Data are averages from 2 independent biological replicates. Error bars show ±SD. Abbreviations: Form, formate; Pepc, phosphoenolpyruvate carboxylase; Pfl, pyruvate formate lyase; PTS, phosphotransferase system.

phenylalanine and tyrosine were consistent with their production via the shikimate pathway (Fig. S2D).

Although the genes encoding the enzymes responsible for producing serine from 3PG are not annotated in *T. saccharolyticum*, our data indicated that serine was produced primarily from 3PG (Fig. 6A and Fig. S3A and B). However, serine can also be synthesized from glycine via serine hydroxymethyltransferase (Shmt; 5,10-methylenetetrahydrofolate [MeTHF] + glycine→serine + tetrahydrofolate; *Tsac_1185* [22, 23]), and our data suggested that a measurable portion of the serine pool (i.e., ~22%) was derived (either net production or exchange) from glycine via Shmt (Fig. 6A and Fig. S3A and B).

Glycine was unlabeled during growth on [6-$^{13}C_1$]glucose and [1-$^{13}C_1$]glucose, consistent with its production either via threonine aldolase (Thra; threonine→glycine + acetaldehyde; *Tsac_0783* [22, 23]) or reverse Shmt (Fig. 6A and Fig. S3A). However, the production of a small fraction (3.6% during [6-$^{13}C_1$]glucose labeling) of M + 2 methionine when only M + 1 aspartate was present indicated that at least some glycine was produced via reverse Shmt to generate ^{13}C-labeled C1 units, from the third carbon in serine, in MeTHF, which can be converted to 5-methyltetrahydrofolate (MTHF) and used to produce M + 2 methionine from M + 1 aspartate (Fig. 6A and Fig. S3A). ^{13}C labeling of C1 units (9.2% M + 1 during [6-$^{13}C_1$]glucose labeling) in 10-formyltetrahydrofolate (FTHF) was also apparent from labeling patterns in purine nucleotides (Fig. S3C).

T. saccharolyticum has annotated genes encoding most of the enzymes required for isoleucine biosynthesis from threonine, but it does not have an annotated threonine deaminase, which is the first step in this pathway. Similarly, most of the enzymes required for isoleucine synthesis via citramalate are annotated, but citramalate synthase is missing (22, 23). Of these routes, the citramalate pathway (49) was necessary to explain isoleucine labeling patterns (Fig. 6B). During [1,2-$^{13}C_2$]glucose labeling, the production of M + 6 isoleucine can only be explained by citramalate pathway activity, and the close to equal proportions of M + 0 to M + 6 and M + 2 to M + 4 labeled forms also support isoleucine production via this pathway. Labeling using an equimolar mixture of [U-$^{13}C_6$]glucose and unlabeled glucose supported primary production of isoleucine via the citramalate pathway and indicated that less than 10% of isoleucine was synthesized from threonine (Fig. S3D).

Reversibility of glycolytic reactions. Having reconstructed the central metabolic network of *T. saccharolyticum*, we sought to compare the reversibility of glycolytic reactions in *T. saccharolyticum* to those in *C. thermocellum* to identify potential factors influencing the greater ethanol productivity in *T. saccharolyticum*. As previously detailed in the introduction, the glycolytic pathway in *C. thermocellum* has several features that set it apart from the canonical EMP glycolytic pathway, including distinct cofactor utilization at specific steps in the pathway and the use of alternative routes for the conversion of PEP to pyruvate (Fig. 1). We hypothesized that the nonstandard glycolytic pathway of *C. thermocellum* will display substantial differences in reaction reversibility and thermodynamics compared to those of the canonical EMP glycolytic pathway, such as that possessed by *T. saccharolyticum*. We used ^{13}C and ^2H steady-state labeling experiments to directly compare reaction reversibility between the glycolytic pathways of *C. thermocellum*, *T. saccharolyticum*, and anaerobically grown *Escherichia coli* as an additional point of reference.

(i) Reversibility of upper glycolysis (glucose to glyceraldehyde-3-phosphate). Labeling with an equimolar mix of [U-$^{13}C_6$]glucose (M + 6, all carbons are ^{13}C labeled) and unlabeled glucose (M + 0, all carbons are ^{12}C) revealed substantial differences in the reversibility of upper glycolytic reactions between *C. thermocellum*, *T. saccharolyticum*, and *E. coli* (Fig. 7). In this labeling experiment, forward phosphofructokinase activity (i.e., F6P→FBP) will first produce a 50:50 mixture of fully labeled (M + 6) and unlabeled (M + 0) FBP. However, as DHAP and GAP are ~50% M + 0 and ~50% M + 3 labeled, reverse flux from Fba will produce a 25:50:25 mixture of M + 6, M + 3, and M + 0 FBP. Therefore, the production of M + 3 FBP provides a measure of the *in vivo* reversibility of the Fba reaction. The fractions of M + 3 FBP in *C. thermocellum*, *T.*
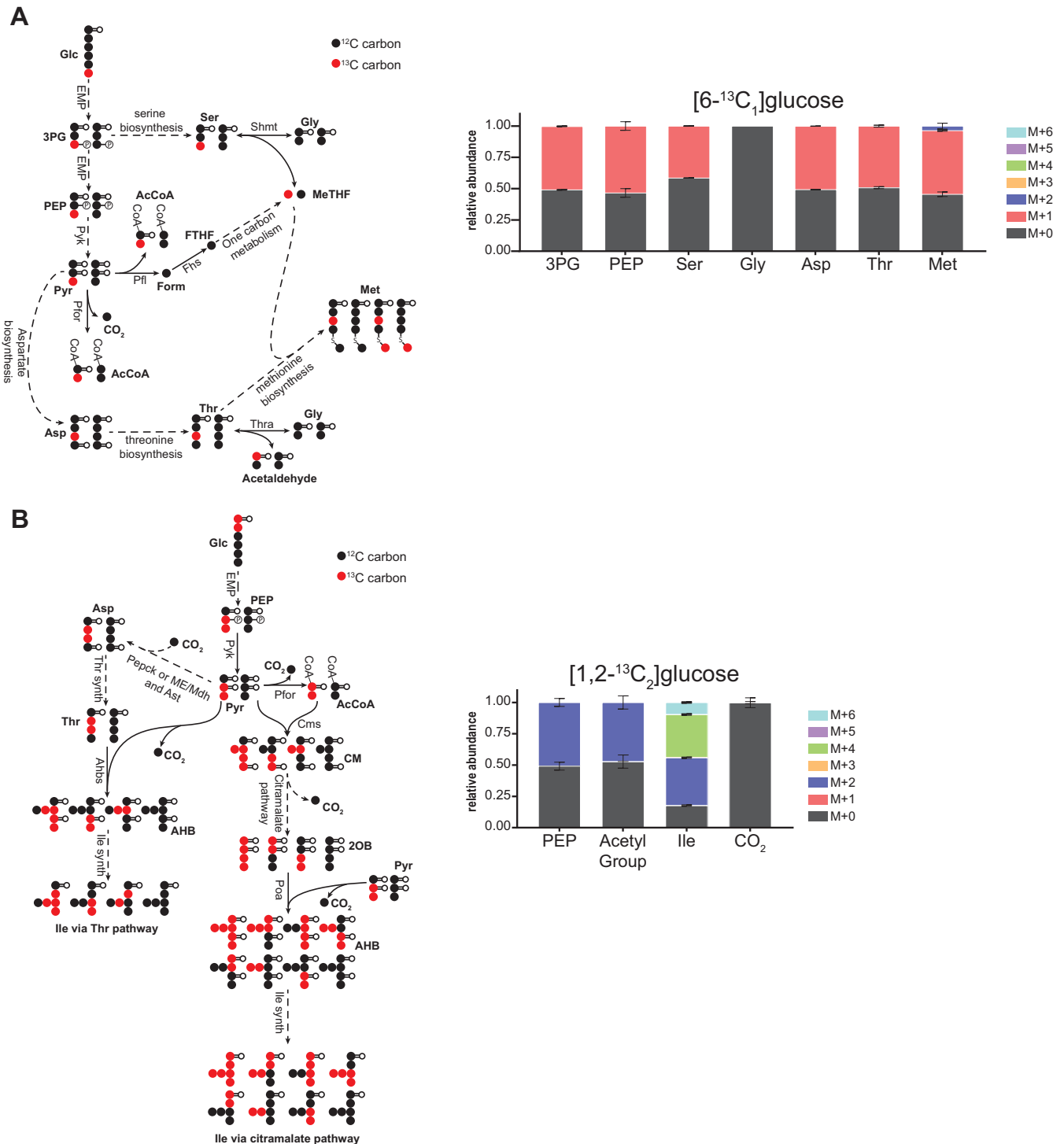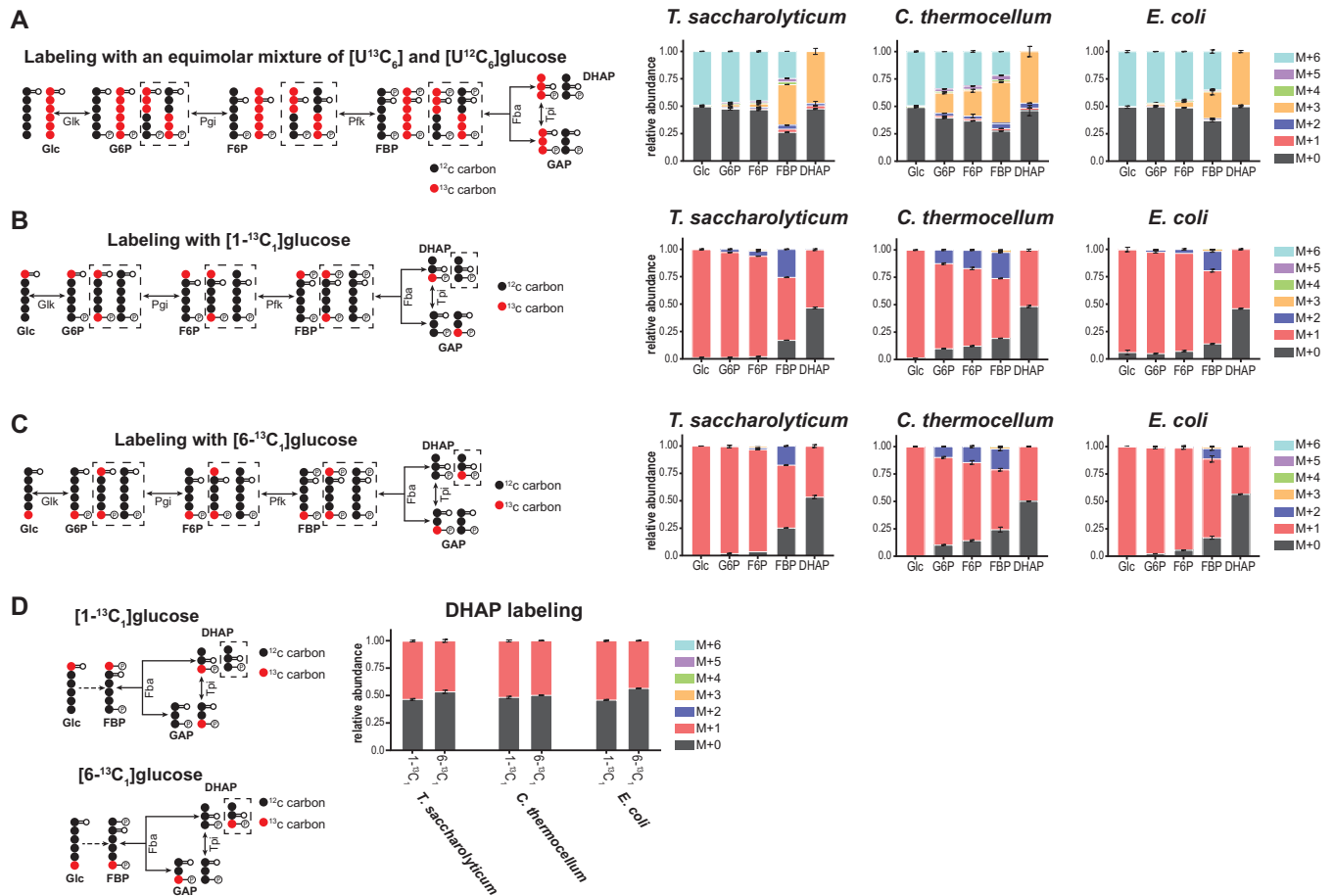
FIG 6 One carbon metabolism and aromatic amino acid production. (A) [6-^{13}C$_1$]glucose labeling indicated that in *T. saccharolyticum* serine was produced from both 3PG and glycine. In addition, the production of a small fraction of M + 2 methionine indicated the presence of ^{13}C-labeled C1 units in 5-methyltetrahydrofolate (MTHF), which is produced from 5,10-methylenetetrahydrofolate (MeTHF). This implied partial production of C1 units from serine via SMHT. These conclusions were supported by [1-^{13}C$_1$] and [1,2-^{13}C$_2$]glucose labeling data (Fig. S3). (B) Isoleucine may be produced from threonine or via the citramalate pathway. [1,2-^{13}C$_2$]glucose labeling data were consistent with production of isoleucine via the citramalate pathway in *T. saccharolyticum*. Specifically, production of M + 6 isoleucine can only be explained by citramalate pathway activity, and the close-to-equal proportions of M + 0 to M + 6 and M + 2 to M + 4 labeled forms also support isoleucine production via this pathway. Labeling experiments using an equimolar mixture of [U-^{13}C$_6$]glucose and [U-^{12}C$_6$]glucose supported this conclusion (Fig. S3D). CO$_2$ labeling was inferred from the MIDs of citrulline and ornithine. The diagrams on the left show predicted metabolite labeling with the specified isotope tracer. Solid arrows represent a single reaction; dashed arrows represent multiple reaction steps. ^{13}C-labeled carbons are colored red; ^{12}C-labeled carbons are colored black. Data are averages from 2 or 3 independent biological replicates. Error bars show ±SD. Pyruvate formate lyase (Pfl) was omitted from panels A and B for clarity but serve the same role as Pfor. Abbreviations: 2OB, 2-oxobutanoate; AHB, acetohydroxybutanoate; Ahbs, acetohydroxybutanoate synthase; CM, citramalate; Cms, citramalate synthase; Fhs, formate tetrahydrofolate ligase; FTHF, 10-formyltetrahydrofolate; Gly, glycine;

(Continued on next page)

FIG 7 ^{13}C labeling reveals reversibility of upper glycolytic reactions. (A, B, and C) Steady-state labeling patterns of upper glycolytic intermediates in *C. thermocellum*, *T. saccharolyticum*, and *E. coli* during anaerobic growth on an equimolar mixture of [U-^{13}C$_6$]- and [U-^{12}C$_6$]glucose (A), [1-^{13}C$_1$]glucose (B), or [6-^{13}C$_1$]glucose (C). The production of M + 3 FBP in panel A or M + 2 and M + 0 FBP in panels B and C indicated high reversibility of the Fba reaction in all three bacteria. Large differences in the reverse propagation of M + 3 FBP (A) or M + 2 and M + 0 FBP (B and C) to F6P suggested that the Pfk reaction was substantially more reversible in *C. thermocellum* than *T. saccharolyticum* or *E. coli*. (D) The reversibility of triose phosphate isomerase (Tpi) was revealed by [6-^{13}C$_1$]glucose and [1-^{13}C$_1$]glucose labeling. During [6-^{13}C$_1$]glucose labeling, forward Fba activity first produces M + 0 DHAP. However, reverse Tpi flux results in the production of M + 1 DHAP from M + 1 GAP. Thus, the closer the M + 1 DHAP fraction is to 50%, the more reversible the Tpi. Labeling data indicated that Tpi was most reversible in *C. thermocellum*, with a proportion of M + 1 DHAP approaching 50% under both the [1-^{13}C$_1$]glucose and [6-^{13}C$_1$]glucose conditions. *T. saccharolyticum* had a less reversible Tpi reaction, followed by *E. coli*, which had a significant enrichment of M + 1 DHAP under the [1-^{13}C$_1$]glucose condition and an enrichment of M + 0 DHAP under the [6-^{13}C$_1$]glucose condition. The diagrams on the left depict predicted metabolite labeling. Solid arrows represent a single reaction; dashed arrows represent multiple reaction steps. ^{13}C-labeled carbons are colored red; ^{12}C-labeled carbons are colored black. Dashed boxes indicate metabolite-labeled forms produced by reverse flux. Data are averages from 2 or 3 independent biological replicates. Error bars show ±SD.

FIG 6 Legend (Continued)

Ile, isoleucine; KIV, keto-isovalerate; Met, methionine; MeTHF, 5,10-methylenetetrahydrofolate; Poa, pyruvate oxobutanoate acetaldehyde transferase; Ser, serine; Shmt, serine hydroxymethyltransferase; THF, tetrahydrofolate; Thr, threonine; Thra, threonine aldolase.

saccharolyticum, and *E. coli* were ~38%, ~37%, and ~24%, respectively, indicating that Fba is highly reversible in all three organisms but significantly less so in *E. coli* ($P < 0.05$) (Fig. 7A). Once produced, M + 3 FBP may propagate back to F6P and G6P. Therefore, the reversibility of the upstream reactions with Pfk and phosphoglucose isomerase (Pgi; G6P→F6P) is informed by the production of M + 3 F6P and M + 3 G6P. The substantially larger M + 3 F6P fraction in *C. thermocellum* (~23%) versus *T. saccharolyticum* (~3%) and *E. coli* (~5%) indicates that phosphofructokinase is substantially more reversible in this bacterium ($P < 0.005$). This observation is consistent with PP$_i$-Pfk in *C. thermocellum* being less energetically favorable than the ATP-Pfk used by *T. saccharolyticum* and *E. coli* (20, 25, 50, 51). As shown in Fig. 7B and C, differences in the reversibility of the Pfk and Fba reactions across the three bacteria were also evident

from the production of M + 0 and M + 2 FBP and F6P during [1-^{13}C$_1$]- and [6-^{13}C$_1$]glucose labeling.

Reversibility of triose phosphate isomerase (Tpi; DHAP→GAP) was revealed by [6-^{13}C$_1$]- and [1-^{13}C$_1$]glucose labeling (Fig. 7D). For example, during [6-^{13}C$_1$]glucose labeling, forward Fba activity first produces M + 0 DHAP and M + 1 GAP. Forward Tpi activity then produces M + 0 GAP from M + 0 DHAP. However, reverse Tpi flux results in the production of M + 1 DHAP from M + 1 GAP. Thus, the closer the M + 1 DHAP fraction is to 50%, the closer Tpi is to equilibrium (i.e., equal forward and reverse flux). The fractions of M + 1 DHAP in *C. thermocellum*, *T. saccharolyticum*, and *E. coli* were 49.8%, 46.4%, and 43.5%, respectively, indicating that Tpi is highly reversible in all three organisms. The data indicated that Tpi was significantly more reversible in *C. thermocellum* than *E. coli* ($P < 0.005$), although the difference between *C. thermocellum* and *T. saccharolyticum* did not reach statistical significance ($P = 0.07$).

(ii) Reversibility of lower glycolysis (GAP to PEP). ^{2}H tracers can provide information on the reversibility of reactions where a C-H bond is broken or formed via dehydration, isomerization, or dehydrogenation (27–29). Hence, we used [4-^{2}H$_1$]glucose and [5-^{2}H$_1$]glucose for investigating reversibility of lower glycolytic reactions (i.e., GAP to PEP) in which carbon rearrangements do not occur.

As shown in Fig. 8A, during [4-^{2}H$_1$]glucose labeling, [1-^{2}H$_1$]GAP (i.e., GAP with a deuterium atom bound to its first carbon) is produced via Fba. Conversion of [1-^{2}H$_1$]GAP to 1,3-bisphosphoglycerate (BPG), catalyzed by glyceraldehyde-3-phosphate dehydrogenase (GAPDH), removes the deuterium from [1-^{2}H$_1$]GAP and places it on NAD$^+$, generating ^{2}H-labeled NADH. Reverse GAPDH flux then can produce unlabeled GAP if unlabeled NADH is used. The M + 0 GAP produced can propagate to DHAP (via reverse Tpi) and FBP (via reverse Fba), as well as to other upstream glycolytic intermediates. We observed that during growth on [4-^{2}H$_1$]glucose, *C. thermocellum* displayed a larger loss of ^{2}H labeling across all glycolytic intermediates than *T. saccharolyticum* and *E. coli*, which indicated increased reversibility of glycolytic reactions in this bacterium. For example, although we could not reliably measure GAP, higher fractions of M + 0 DHAP and M + 0 FBP in *C. thermocellum*, i.e., 92% and 72%, respectively, versus 82% and 62% in *T. saccharolyticum* or 89% and 43% M + 0 in *E. coli*, suggested greater reversibility of its GAPDH/Tpi and GAPDH/Fba pairs of reactions ($P < 0.05$ for all pairwise comparisons).

During growth on [5-^{2}H$_1$]glucose, the intermediates GAP, BPG, 3PG, and 2-phosphoglycerate (2PG) become deuterated at the second carbon (Fig. 8B). The loss of deuterium can occur from the conversion of [2-^{2}H$_1$]GAP to M + 0 DHAP via reverse Tpi or by the forward phosphopyruvate hydratase reaction (Eno) converting [2-^{2}H$_1$]2PG to M + 0 PEP. Once produced, propagation of M + 0 DHAP or M + 0 PEP to upstream metabolites provides a measure of the reversibility of Tpi, Eno, and other glycolytic reactions. As with [4-^{2}H$_1$]glucose, the greater loss of ^{2}H labeling across glycolytic intermediates in *C. thermocellum* during [5-^{2}H$_1$]glucose labeling indicated increased reversibility of glycolysis in this bacterium compared to that of *T. saccharolyticum* or *E. coli*. For example, taking Tpi reversibility into account (Fig. 7D), the larger fractions of M + 0 3PG in *C. thermocellum* (98.4%) and *T. saccharolyticum* (96.6%) suggested increased reversibility of the Pgm/Eno reaction pair in these thermophilic organisms compared to that in *E. coli* (88.4%; $P < 0.05$ for both pairwise comparisons).

(iii) Reversibility of the conversion of phosphoenolpyruvate to pyruvate. *C. thermocellum* lacks pyruvate kinase (Pyk; PEP + ADP→Pyr + ATP) and instead transforms PEP to Pyr via pyruvate phosphate dikinase (Ppdk; PEP + AMP + PP$_i$→Pyr + ATP + P$_i$) or the malate shunt (Fig. 5). In contrast, Pyr production from PEP in *E. coli* and *T. saccharolyticum* occurs via Pyk or the phosphotransferase system (PTS) (18, 40, 52, 53). On its way toward fermentative pathways, Pyr is decarboxylated by Pfor or Pfl in *C. thermocellum* and *T. saccharolyticum* (6, 24, 54–57). In anaerobically grown *E. coli*, Pyr is converted to acetyl-CoA by Pfl (58, 59).
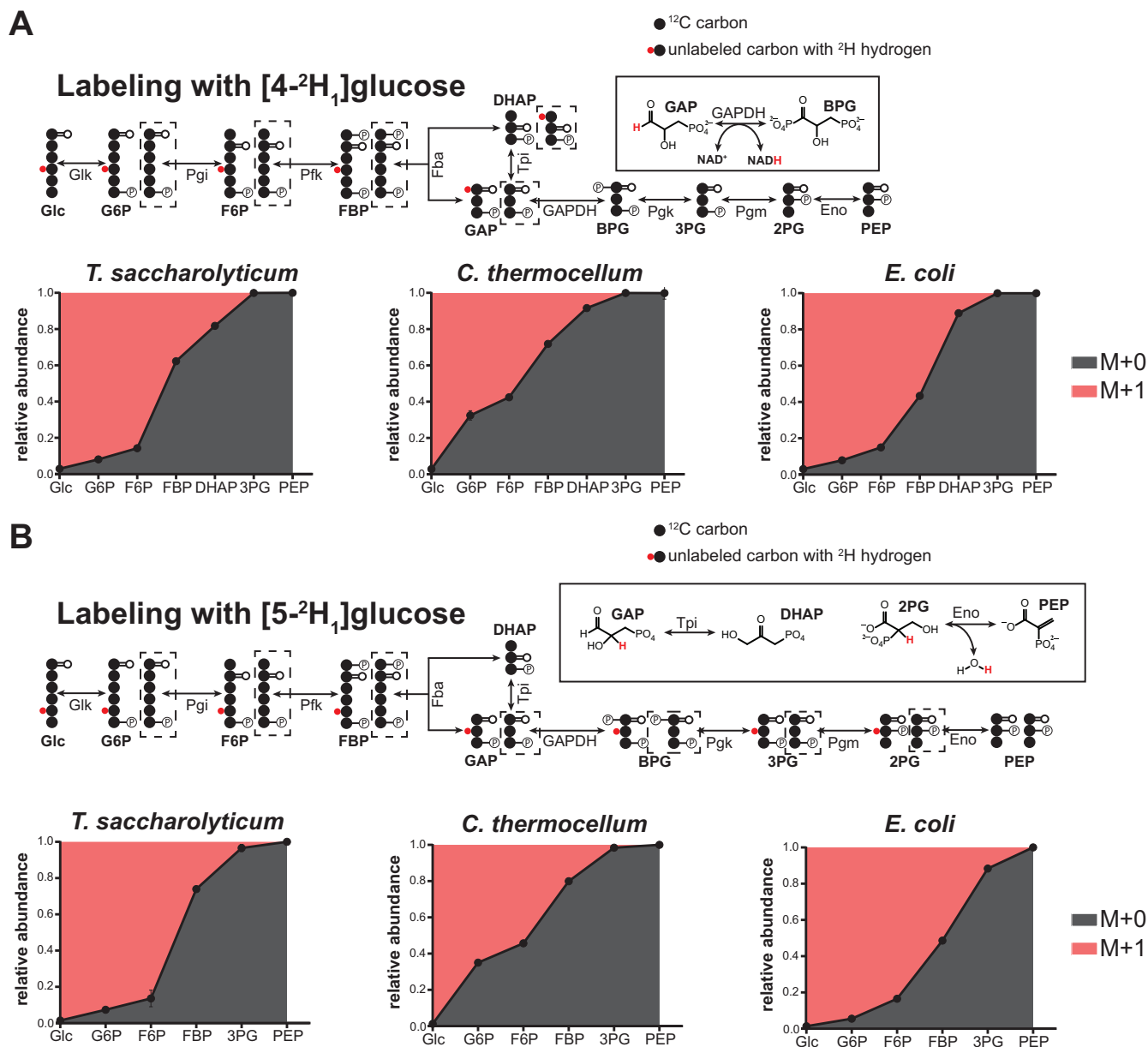
FIG 8 ^{2}H labeling reveals reversibility of upper and lower glycolytic reactions. Steady-state labeling patterns of lower glycolytic intermediates in *C. thermocellum*, *T. saccharolyticum*, and *E. coli* during anaerobic growth on [4-^{2}H]glucose or [5-^{2}H]glucose. (A) During [4-^{2}H$_1$]glucose labeling, GAPDH converts [1-^{2}H$_1$]GAP to unlabeled BPG (the deuteron is transferred to [^{2}H$_1$]NADH). Reverse GAPDH flux then can produce unlabeled GAP if unlabeled NADH is used by the enzyme. The M + 0 GAP produced thusly can propagate to upstream glycolytic intermediates and be used as a measure of the reversibility of GAPDH and upstream reactions. *C. thermocellum* displayed a substantially larger loss of ^{2}H labeling (i.e., greater M + 0 fraction) across glycolytic intermediates (i.e., DHAP, FBP, F6P, and G6P) than *T. saccharolyticum* and *E. coli*, indicating increased reversibility of its glycolytic pathway. (B) During growth on [5-^{2}H$_1$]glucose, GAP, BPG, 3PG, and 2PG become deuterated at the second carbon. Conversion of [2-^{2}H$_1$]2PG to unlabeled PEP results in the loss of deuterium to water. The propagation of unlabeled PEP to upstream intermediates then indicates the reversibility of upstream reactions. The deuterium in [2-^{2}H$_1$]GAP also may be lost during its conversion to DHAP. *C. thermocellum* displayed a substantially larger loss of ^{2}H labeling across all glycolytic intermediates than *T. saccharolyticum* and *E. coli*, indicating once again the increased reversibility of its glycolytic reactions. The diagrams on the left depict predicted metabolite labeling. Solid arrows represent a single reaction; dashed arrows represent multiple reaction steps. ^{12}C carbons are colored black; deuterons (^{2}H) are depicted as small red circles. Dashed boxes indicate metabolite-labeled forms produced via reverse flux. The chemical reactions enclosed in solid boxes in panels A and B illustrate the step in the pathway at which the loss of deuterium occurs. Data are averages from 2 or 3 independent biological replicates. Error bars show ±SD. Error bars smaller than the icon used to represent the average are not visible.

When cells are grown in an equimolar mixture of [U-^{13}C$_6$]glucose and unlabeled glucose, the Pyr initially produced via glycolysis is either M + 0 or M + 3, and its decarboxylation produces acetyl-CoA containing an M + 0 or M + 2 acetyl group. Complete or partial (i.e., decarboxylation step only) reversibility of Pfor or Pfl resulted in the interchange of the carboxylic group in Pyr with unlabeled CO$_2$ or formate to

produce M + 2 Pyr (60) (Fig. 5). Pyr decarboxylation was significantly more reversible in *E. coli* (33.2% M + 2 Pyr) and *C. thermocellum* (26.5% M + 2 Pyr) than in *T. saccharolyticum* (14.8% M + 2 Pyr; $P < 0.05$ for both pairwise comparisons).

Once formed, M + 2 Pyr may propagate to upstream metabolites to produce M + 2 PEP, indicating reversibility of PEP-to-Pyr conversion by whichever route the organism has available. Despite a potentially longer path, we observed that PEP-to-Pyr conversion was significantly more reversible ($P < 0.01$) in *C. thermocellum* (10.2% M + 2 PEP) than in *E. coli* (2.0% M + 2 PEP). Data suggested that PEP-to-Pyr conversion was also more reversible in *C. thermocellum* than *T. saccharolyticum* (3.9% M + 2 PEP), but this difference was not significant at $P < 0.05$. Considering the reported absence of pyruvate carboxylase or oxaloacetate decarboxylase activity in *C. thermocellum* (18, 26), the production of M + 2 Mal (14.0%) and M + 2 aspartate (12.0%; surrogate for OAA) suggested considerable reversibility of the malate shunt. Another potential alternative for the production of M + 2 aspartate and M + 2 Mal in *C. thermocellum* is a reversible citrate synthase, which has been shown to be reversible in other thermophilic bacteria, such as *Desulfurella acetivorans* and *Thermosulfidibacter takaii* (61, 62).

(iv) Reversibility of ethanol production from pyruvate. Since *C. thermocellum* and *T. saccharolyticum* are being developed for the production of ethanol from lignocellulosic biomass, we were interested in investigating the reversibility of their ethanol fermentation pathways in addition to glycolysis. In both *C. thermocellum* and *T. saccharolyticum*, acetyl-CoA, produced from Pyr, is reduced to acetaldehyde [AcCoA + NAD(P)H→acetaldehyde + NAD(P)$^+$] and then to ethanol [acetaldehyde + NAD-(P)H→ethanol + NAD(P)$^+$] by a bifunctional aldehyde/alcohol dehydrogenase, AdhE (15). *T. saccharolyticum* also possesses an NADPH-dependent alcohol dehydrogenase (AdhA) (16). To investigate the reversibility of the Pyr-to-ethanol pathway, we grew *C. thermocellum* and *T. saccharolyticum* in the presence of [1-^{13}C$_1$]ethanol and unlabeled cellobiose (for *C. thermocellum*) or unlabeled glucose (for *T. saccharolyticum*). The incorporation of ^{13}C from [1-^{13}C$_1$]ethanol into acetyl-CoA was significantly larger ($P < 0.005$) in *C. thermocellum* (67.9% M + 1) than *T. saccharolyticum* (46.0% M + 1), indicating increased reversibility of the conversion of acetyl-CoA to ethanol in *C. thermocellum* (Fig. 9). Additionally, Pyr was 21.3% M + 1 labeled in *C. thermocellum* but only 1.7% M + 1 labeled in *T. saccharolyticum*, indicating a significantly less reversible Pfor/Pfl reaction in *T. saccharolyticum* ($P < 0.01$). We also observed significant propagation of ^{13}C from [1-^{13}C$_1$]ethanol into upper glycolytic intermediates, such as G6P (5.5% M + 1) and FBP (8.8% M + 1), in *C. thermocellum* ($P < 0.05$ for both metabolites). However, these metabolites remained essentially unlabeled in *T. saccharolyticum* (<0.2% M + 1). Overall, this analysis indicated a substantially more reversible ethanol fermentation pathway in *C. thermocellum* than *T. saccharolyticum*.

^{2}H and ^{13}C metabolic flux analysis. To determine *in vivo* flux ratios (J^+/J^-) and compare the thermodynamics of the distinct glycolytic pathways of *C. thermocellum* and *T. saccharolyticum*, we integrated data from five ^{13}C and ^{2}H tracer experiments ([1-^{13}C$_1$]-, [6-^{13}C$_1$]-, [4-^{2}H$_1$]-, [5-^{2}H$_1$]glucose, and an equimolar mixture of [U-^{13}C$_6$]glucose and unlabeled glucose) into a single flux map for each organism (Fig. 10A and Table S2). MFA was performed using the INCA software suite, which utilizes the elementary metabolite unit (EMU) framework to model isotopic distributions (63, 64). Reaction directionalities were not predetermined for most reactions in central carbon metabolism (glycolysis, TCA cycle, and PPP) to allow combined ^{2}H and ^{13}C MFA to determine forward and reverse fluxes. Reaction directionality was preassigned primarily for transport reactions, dilution fluxes, and combined amino acid biosynthesis reactions.

For *T. saccharolyticum*, ^{2}H and ^{13}C MFA best-fit solutions validated the qualitative assessment of its metabolic network, presented earlier. We constructed alternative models containing all possible glycolytic routes (e.g., EMP, ED, and oxidative pentose phosphate pathways) as well as models lacking reactions that we identified as necessary to explain labeling patterns of specific metabolites (e.g., citramalate pathway for
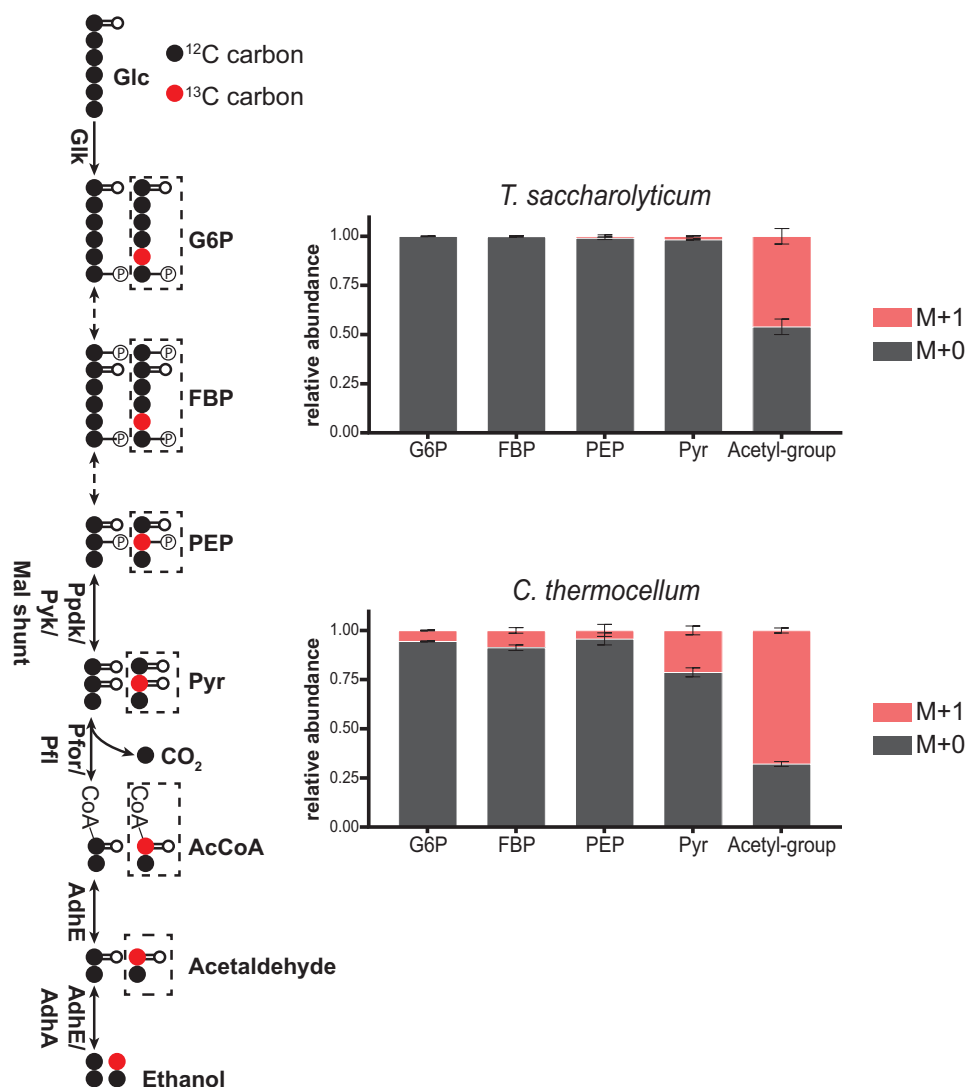
FIG 9 Reversibility of the pyruvate-to-ethanol pathway in *C. thermocellum* and *T. saccharolyticum*. Steady-state labeling with [1-^{13}C$_1$]ethanol in *C. thermocellum* and *T. saccharolyticum* revealed that the pyruvate-to-ethanol pathway in *C. thermocellum* was substantially more reversible than that of *T. saccharolyticum*. Reversibility of the AdhA and AdhE reactions resulted in ^{13}C-labeled AcCoA (at the acetyl group), which was more labeled in *C. thermocellum* than in *T. saccharolyticum*. Reverse activity of Pfor or Pfl resulted in the production of M + 1 pyruvate. Reverse activity of EMP reactions above pyruvate resulted in the production of labeled glycolytic intermediates. The diagrams on the left depict predicted metabolite labeling. Solid arrows represent a single reaction; dashed arrows represent multiple reaction steps. ^{13}C-labeled carbons are colored red; ^{12}C-labeled carbons are colored black. Dashed boxes indicate metabolite-labeled forms produced by reverse flux. Data are averages from 3 independent biological replicates. Error bars show ±SD. Abbreviations: AdhA, alcohol dehydrogenase; AdhE, bifunctional alcohol/aldehyde dehydrogenase.

isoleucine production and SBP bypass for S7P production). The results of this analysis agreed with our previous conclusions and predicted an inactive ED pathway (i.e., <0.25% glycolytic flux), an inactive oxidative PPP (i.e., 0% flux), and a bifurcated TCA cycle with oxidative production of AKG and reductive production of succinate. Although Pepck typically is considered a gluconeogenic reaction (i.e., transforming OAA to PEP), our MFA results supported the activity of a PEP carboxylating enzyme producing OAA from PEP. We also found that the SBP bypass was necessary to explain labeling patterns in PPP intermediates and aromatic amino acids. This analysis also supported qualitative conclusions regarding amino acid biosynthetic routes, such as isoleucine synthesis via the citramalate pathway instead of from threonine. Additionally, the production of serine from 3PG and its
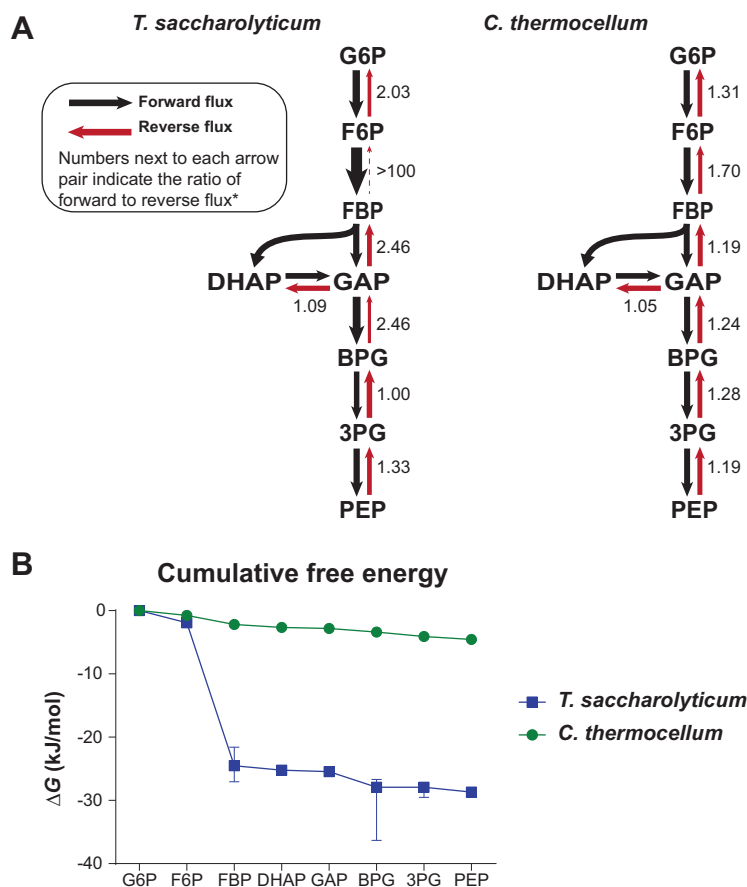
FIG 10 Glycolytic reversibility in *C. thermocellum* and *T. saccharolyticum*. (A) Flux maps for *C. thermocellum* and *T. saccharolyticum* during glucose fermentation were generated by simultaneously fitting data from five parallel ^{13}C and ^{2}H tracer experiments (i.e., [1-$^{13}C_1$]glucose, [6-$^{13}C_1$]glucose, [4-$^{2}H_1$]glucose, [5-$^{2}H_1$]glucose, and an equimolar mixture of [U$^{13}C_6$]glucose and unlabeled glucose) into a single, statistically acceptable flux map. Arrow thickness is proportionate to net flux. Numbers next to each arrow represent net flux, with reverse fluxes in parentheses. Fluxes are represented as a proportion of glucose uptake, which was normalized to 100. Malic enzyme was omitted from the *C. thermocellum* model due to the analysis being unable to resolve flux through malic enzyme versus Ppdk. Omission of malic enzyme had a negligible effect on flux ratios in glycolysis (see Materials and Methods). *, see Table S2 for complete MFA results, including 95% confidence intervals. (B) MFA-derived ΔG values for glycolytic reactions (Table 1) revealed that the glycolytic pathway in *C. thermocellum* was remarkably close to thermodynamic equilibrium, with an overall drop in Gibbs free energy of -4.55 kJ/mol between G6P and PEP. In contrast, the overall drop in free energy of glycolysis in *T. saccharolyticum* was substantially greater, $\Delta G = -28.67$ kJ/mol. The limited thermodynamic driving force of the glycolytic pathway in *C. thermocellum* could be attributed in large part to the small driving force of the Pfk reaction, which had a ΔG of only -1.45 kJ/mol compared to -22.57 kJ/mol in *T. saccharolyticum*. Intracellular metabolite concentrations provided cross-validation of ΔG estimates for the Pfk reaction in *T. saccharolyticum* (see Materials and Methods). Error bars shown represent the 95% confidence intervals of the free energy estimates. Error bars smaller than the icon used to represent the average are not visible.

consumption by Shmt to form labeled THF intermediates was necessary to achieve a statistically acceptable model fit.

For *C. thermocellum*, our MFA results were also consistent with the previously reported central metabolic network (26). Specifically, our analysis predicted glycolysis via the EMP pathway with no ED pathway activity, a solely nonoxidative PPP containing a SBP bypass, and a bifurcated TCA cycle. Our results were also consistent with reported amino acid synthesis pathways in *C. thermocellum*.

Comparative thermodynamic pathway analysis. Using the relation $\Delta G = -RT$ $\ln(J^+/J^-)$, we estimated ΔG of glycolytic reactions (i.e., from G6P to PEP) from MFA-derived flux ratios (J^+/J^-) in *C. thermocellum* and *T. saccharolyticum* (Fig. 10B and

TABLE 1 Reaction free energies calculated from integrated ^{13}C and ^{2}H MFA-derived fluxes in *C. thermocellum* and *T. saccharolyticum*

	ΔG in:					
	C. thermocellum			*T. saccharolyticum*		
Glycolytic reaction	Best fit	LB[b]	UB[b]	Best fit	LB	UB
G6P + H↔F6P + H	−0.74	−0.67	−0.81	−1.93	−1.62	−2.25
F6P↔FBP[a]	−1.45	−1.40	−1.49	−22.57	−19.67	−25.11
FBP + H↔DHAP + GAP	−0.47	−0.45	−0.50	−0.70	−0.43	−1.18
DHAP + H↔GAP + H	−0.14	−0.12	−0.16	−0.24	−0.20	−0.30
GAP + NAD↔BPG + NADH	−0.59	−0.20	−1.14	−2.46	−1.25	−10.87
BPG↔3PG	−0.67	−0.13	−1.07	0.00	0.00	−1.63
3PG↔PEP + H	−0.48	−0.30	−0.71	−0.77	−0.51	−1.26

[a]The F6P↔FBP reaction free energy for *T. saccharolyticum* is calculated from our measured intracellular metabolite concentrations, because the MFA-derived free energy was unbounded in the negative direction.
[b]LB and UB are the lower and upper bounds defined by a 95% confidence interval for the free energy.

Table 1). For a small number of reactions, we used intracellular metabolite concentrations to improve ΔG estimates obtained from MFA-derived flux ratios (Table 1). Estimated ΔG values aligned with the qualitative assessment of reaction reversibility presented above and showed that the glycolytic pathway in *C. thermocellum*, with an overall ΔG of −4.55 kJ/mol, operates remarkably close to thermodynamic equilibrium. In comparison, the glycolytic pathway in *T. saccharolyticum* was substantially more thermodynamically favorable (overall ΔG = −28.67 kJ/mol) and was comparable to the glycolytic pathway in anaerobically grown *E. coli* (overall ΔG = −23.47 kJ/mol) (29) (Fig. S4).

The limited thermodynamic driving force of the glycolytic pathway in *C. thermocellum* could be attributed in large part to the small driving force of the Pfk reaction, which had a ΔG of only −1.45 kJ/mol compared to −22.57 kJ/mol in *T. saccharolyticum* and −18.84 kJ/mol in *E. coli*. The small ΔG of Pfk in *C. thermocellum* was likely due to the use of PP_i instead of ATP as the high-energy phosphate donor. Indeed, the standard free energy for the ATP-dependent Pfk (ΔG = −15.0 kJ/mol) is ~10.6 kJ/mol more favorable than the PP_i-dependent Pfk (ΔG = −4.4 kJ/mol) due to the greater free energy of ATP hydrolysis than PP_i hydrolysis (50).

Consistent with our qualitative observations regarding its reversibility, the Fba reaction operated close to thermodynamic equilibrium in both *T. saccharolyticum* (−0.70 kJ/mol) and *C. thermocellum* (−0.47 kJ/mol) but was more thermodynamically favorable in anaerobic *E. coli* (−3.64 kJ/mol) (29). Also in agreement with qualitative observations, the Pgi reaction was slightly more favorable in *T. saccharolyticum* (−1.93 kJ/mol) than in *C. thermocellum* (−0.74 kJ/mol). The ΔG of lower glycolytic reactions (GAPDH to Eno) were close to equilibrium in both *C. thermocellum* and *T. saccharolyticum* but were generally more favorable in *T. saccharolyticum*. For example, the ΔG of the Pgm/Eno pair of reactions was −0.49 kJ/mol in *C. thermocellum* compared to −0.77 kJ/mol in *T. saccharolyticum*.

In both *C. thermocellum* and *T. saccharolyticum*, most of the reactions in the PPP, including Sba, SBPase, Rpi, and Rpe, as well as the transketolase half reactions TktA (Xu5P→GAP + C2) and TktB (S7P→R5P + C2), all had ΔG no more favorable than −1.3 kJ/mol, putting them close to thermodynamic equilibrium (Table S3).

DISCUSSION

Metabolite concentrations and thermodynamics of glycolysis. Intracellular concentrations of glycolytic intermediates across the bacteria in this study reflected the thermodynamic profile of their glycolytic pathways (see Table S1). For example, the limited driving force of the PP_i-Pfk reaction in *C. thermocellum* was associated with a low FBP concentration, which was about one-third of that in *T. saccharolyticum* or *E. coli*. In contrast, G6P and F6P levels in *C. thermocellum* were higher than those in *T. saccharolyticum* (6.8-fold and 1.2-fold, respectively) and also higher than those in *E. coli* (4.1-fold and 5.0-fold, respectively). Higher levels of G6P and F6P in *C. thermocellum*

potentially reflect the need to accumulate larger amounts of upper glycolytic intermediates to drive the PP$_i$-Pfk reaction forward. Indeed, the FBP/F6P ratio was considerably lower in *C. thermocellum* ($\sim$1) than *E. coli* ($\sim$15) or *T. saccharolyticum* ($\sim$3.7). Thus, higher intracellular FBP concentrations maintained by the more favorable upper EMP reactions in *E. coli* and *T. saccharolyticum* may help drive subsequent reactions in glycolysis.

Interestingly, ATP/ADP and GTP/GDP ratios were considerably lower in *C. thermocellum* (25.7 and 28.7, respectively) than *E. coli* (66.0 and 42.4) and *T. saccharolyticum* (59.9 and 61.4). The higher ATP/ADP ratios in *E. coli* and *T. saccharolyticum* likely contribute to the favorability of the ATP-Pfk reaction and other reactions in upper glycolysis in these organisms. In contrast, the low ATP/ADP and GTP/GDP ratios in *C. thermocellum* may help make ATP/GTP-generating reactions in lower glycolysis, such as GAPDH and Ppdk, more favorable but may also slow biosynthetic reactions that rely on ATP/GTP hydrolysis, such as amino acid, protein, fatty acid, nucleotide, and mRNA synthesis.

Enzyme efficiency, metabolic flux, and product titers. Thermodynamics constitutes a key determinant of enzyme efficiency and flux within metabolic pathways. As determined by $\Delta G = -RT \ln(J^+/J^-)$, enzyme efficiency (i.e., the fraction of enzyme used in the forward versus reverse direction) is directly proportional to the drop in Gibbs free energy (ΔG) of a biochemical reaction (31, 32). Thus, the fraction of enzyme that counterproductively catalyzes the reverse reaction (J^-) increases exponentially as ΔG approaches equilibrium, decreasing the net reaction rate ($J^+ - J^-$) (33, 65). This implies that a metabolic pathway that is close to thermodynamic equilibrium will require substantially greater amounts of catalytically active enzyme to maintain a given flux than a more thermodynamically favorable pathway. Therefore, considering cellular limits on total enzyme abundance (66), the small thermodynamic driving force of *C. thermocellum* glycolysis could represent a limiting factor for engineering ethanologen strains with high glycolytic rates.

Besides limiting flux, a small thermodynamic driving force also can make a pathway more susceptible to end product inhibition, since only a comparatively small amount of product would need to accumulate before some reaction within the pathway approaches thermodynamic equilibrium ($\Delta G \rightarrow 0$) and effectively stops further substrate utilization and product formation. Therefore, it is likely that the limited thermodynamic driving force of the *C. thermocellum* glycolytic pathway represents a key contributor to its low ethanol titer (25 g/liter) (6) compared to that of organisms with more thermodynamically favorable glycolysis, such as *T. saccharolyticum* (70 g/liter) (3), *S. cerevisiae* (75 g/liter) (67), and *Z. mobilis* ($>$85 g/liter) (27, 68, 69). Indeed, a recent computational evaluation that used maximum-minimum driving force (MDF)-based analysis to model the thermodynamics of the glycolytic and ethanol fermentation pathways in *C. thermocellum* predicted that the thermodynamic driving force of these pathways is rapidly depleted as ethanol accumulates extracellularly (70). This limitation may help explain the difficulties encountered by groups attempting to engineer *C. thermocellum* to increase product titers compared to the successes at engineering *T. saccharolyticum* (6, 10, 13, 16, 70).

Our results suggest that a promising strategy for increasing glycolytic flux and ethanol titers in *C. thermocellum* is to replace PP$_i$-Pfk with an ATP-dependent Pfk. In addition, replacing the malate shunt and Ppdk routes for conversion of PEP to Pyr with Pyk also may increase flux and ethanol titers by providing a single more thermodynamically favorable route. Indeed, *C. thermocellum* strains expressing an exogenous Pyk achieve higher ethanol titers (13), and elimination of malate shunt activity improved ethanol production in *Clostridium cellulolyticum*, another cellulolytic ethanol producer (71). Finally, adding a mechanism for ATP hydrolysis could increase the thermodynamic favorability of ATP-harvesting reactions in glycolysis (Pgk and Pyk) (31). ATP demand has been implicated in glycolytic flux control in a number of organisms, including *Z. mobilis*, *S. cerevisiae*, and *E. coli*. (72–74). This strategy has a potential additional benefit

in that it may limit cellular resources that are spent on replication by limiting access of biosynthetic reactions to ATP (72, 74).

The previously reported MDF-based analysis of *C. thermocellum* also produced a computationally derived thermodynamic profile of glycolysis (60). Our *in vivo* measurement of pathway free energies agreed with the general thermodynamic profile produced by MDF, with most of the free energy released by the Pfk and Ppdk reactions and the rest of the reactions closer to equilibrium. Although the overall profiles were similar, their analysis predicted more favorable PP_i-Pfk (-6.67 kJ/mol) and Ppdk (-6.92 kJ/mol) reactions than the values we report in this study (-1.45 and -3.35 kJ/mol, respectively). This discrepancy may be due to *in vivo* constraints not accounted for in the MDF analysis, such as limits on enzyme abundance and the need to maintain adequate metabolite pools to drive biosynthetic pathways (31, 33, 34). In addition, the cellular objective in *C. thermocellum* may not be completely aligned with the objective function implicit in the MDF algorithm (i.e., to maximize the lowest free energy given a set of reaction steps).

A trade-off between thermodynamic driving force and energy yield. Interestingly, the limited driving force of the glycolytic pathway in *C. thermocellum* mirrors that of *C. cellulolyticum*, another cellulose-degrading organism that also utilizes PP_i-Pfk, Ppdk, and the malate shunt (29, 71, 75). A potential advantage of glycolytic pathways with low thermodynamic driving force is increased energy efficiency, i.e., increased ATP or GTP yield per glucose. The use of alternative enzymes, such as PP_i-Pfk (which uses PP_i in place of ATP) and Ppdk (which produces ATP from AMP and PP_i), by cellulolytic microbes represents a potential mechanism for increased energy yield. However, recent research suggests that the PP_i needed for glycolysis is in excess of what can be generated as a byproduct of biosynthetic pathways and is instead generated by ATP-consuming glycogen cycling reactions (20). This casts some doubt on the use of PP_i-dependent enzymes as a mechanism of ATP conservation. However, PP_i also could be generated by a membrane-bound proton-pumping pyrophosphatase (PP_iase, *Cthe_1425*), which is transcribed and expressed in *C. thermocellum* (24, 37). The proton gradient required for this process may originate from ferredoxin oxidation by an ion-tranlocating reduced ferredoxin:NAD^+ oxidoreductase (Rnf) (76, 77), with reduced ferredoxin provided by Pfor in the ethanol fermentation pathway (12, 18). Thus, Pfor, Rnf, and PP_iase may work together to harvest additional energy from glycolysis by coupling pyruvate decarboxylation to proton translocation and subsequent PP_i production. Therefore, PP_i generation from a proton gradient represents a potential mechanism for energy conservation and increased ATP yield by a pathway that utilizes PP_i-dependent enzymes.

The use of near-equilibrium glycolytic pathways with increased ATP yield by cellulolytic bacteria may represent an evolutionary adaptation to growth on cellulosic substrates. Specifically, microbes utilizing soluble substrates can maximize either the specific substrate consumption rate (grams of substrate $\times$ gram cells^{-1} hour^{-1}) or the cell yield (grams of cells $\times$ gram substrate^{-1}), the product of which is the specific growth rate (per hour). For microbes growing on cellulosic biomass, however, the specific substrate consumption rate is highly constrained, leading to strong selective pressure for cellulolytic bacteria to maximize the cell yield by increasing glycolytic ATP yield. Conversely, the use of highly thermodynamically favorable pathways with lower ATP yield, such as the ED pathway in *Z. mobilis*, likely represents an adaptation to glucose-rich environments (27, 31, 78).

In conclusion, our analysis revealed that the glycolytic pathway in *C. thermocellum* is remarkably close to thermodynamic equilibrium compared to the glycolytic pathways of *T. saccharolyticum* and *E. coli*. The primary contributor to the large reversibility of glycolysis in *C. thermocellum* is the Pfk reaction, but AdhE in the ethanol fermentation pathway is likely also an important contributor. Our findings help explain the low ethanol titer in *C. thermocellum* and suggest engineering strategies that can be used to increase its ethanol productivity and glycolytic rate.

MATERIALS AND METHODS

Materials. Tracers ([1-$^{13}C_1$]glucose [98 to 99 atom% ^{13}C], [6-$^{13}C_1$]glucose [99 atom% ^{13}C], [1,2-$^{13}C_2$]glucose [99 atom% ^{13}C], [U-$^{13}C_6$]glucose [99 atom% ^{13}C], [4-$^2H_1$]glucose [98 atom% ^2H], [5-$^2H_1$]glucose [98 atom% ^2H], and [1-$^{13}C_1$]ethanol [99 atom% ^{13}C]) were purchased from Cambridge Isotope Laboratories (Andover, MD). All other chemicals were purchased from Sigma-Aldrich (St. Louis, MO).

Strains and growth conditions. Wild-type *C. thermocellum* (DSM1313) was obtained from the DSMZ culture collection. Wild-type *T. saccharolyticum* (JW/YS-485L) was obtained courtesy of Juergen Wiegel, Department of Microbiology, University of Georgia. Fermentations and growth were carried out in MTC (11.56 g/liter morpholine propanesulfonic acid [MOPS] sodium salt, 3 g/liter trisodium citrate, 1.5 g/liter KH_2PO_4, 1.5 g/liter NH_4SO_4, 2.6 g/liter $MgCl_2 \cdot 6H_2O$, 0.13 g/liter $CaCl_2 \cdot 2H_2O$, 0.001 g/liter $FeCl_2 \cdot 4H_2O$, 0.5 g/liter L-cysteine HCl·H_2O, 0.004 g/liter *p*-aminobenzoic acid, 0.002 g/liter biotin, 0.002 g/liter cobalamin, 0.004 g/liter thiamine, and 5 g/liter either glucose or cellobiose; pH 7 for *C. thermocellum* and pH 6.8 for *T. saccharolyticum*).

We grew small cultures (7 to 10 ml) in 15-ml modified Hungate tubes for labeling experiments, intracellular metabolite quantitation, and growth curves. Larger cultures for extracellular metabolite quantitation were grown in 125- to 200-ml pressure bottles, with culture volume never exceeding more than 2/3 the volume of the bottle. Tubes or bottles were filled with medium base containing MOPS solution, sealed with butyl rubber stoppers, made anaerobic using a vacuum manifold, overlaid with N_2 gas (oxygen scrubbed), and autoclaved. Other medium components were prepared, made anaerobic, autoclaved separately, and then added to culture tubes. Before manipulating cultures, syringes were made anoxic by repeatedly drawing and expelling headspace from an anaerobic sealed bottle containing 2.5% cysteine HCl solution. Tubes were placed in a 55°C water bath after inoculation for growth. Growth was quantified by the optical density at 600 nm (OD_{600}) using a Genesys 20 UV-visible spectrophotometer equipped with a tube adapter. Inoculation and sampling of cultures took place using anoxic syringes, and any manipulation that required opening the tube or extended handling took place in an anaerobic chamber (Coy Laboratory) with a 5% CO_2, 5% H_2, 90% N_2 atmosphere under anaerobic conditions ($<$100 ppm O_2).

Escherichia coli RL3000 (MG1655 IlvG$^+$ rph$^+$ pyrE$^+$ ΔglcB) was obtained courtesy of Robert Landick, Department of Bacteriology, University of Wisconsin–Madison (79). All growth, labeling, and metabolite quantitation were carried out in M9 minimal medium (6 g/liter Na_2HPO_4, 3 g/liter NaH_2PO_4, 0.5 g/liter NaCl, 1 g/liter NH_4Cl, 4 g/liter glucose, 0.1 mM $CaCl_2$, 2 mM $MgSO_4$, 0.075 mM $FeCl_3$) at 37°C in stirred flasks in an anaerobic chamber.

Metabolite collection. Working cultures were inoculated anaerobically with a 1:20 or greater dilution from overnight anaerobic cultures containing the same carbon source to an initial OD_{600} of ~0.05. Cells were grown to mid-exponential phase (OD_{600} of 0.40 to 0.5), and then intracellular metabolites were collected inside the anaerobic chamber by vacuum filtration of 5 ml of culture through 0.45-μm hydrophilic nylon filters to separate cells from the media. Filters then were placed cell-side down in 1.5 ml of extraction solvent (40% acetonitrile, 40% methanol, and 20% water) and kept on dry ice to quench metabolism and extract metabolites. Cells were washed off the filter using the solvent, which was collected, vortexed, and then centrifuged for 5 min at 4°C to remove cellular debris, and the supernatant was collected for liquid chromatography-mass spectrometry (LC-MS) analysis. Labeling with positionally labeled ^{13}C and ^2H tracers was performed in biological duplicate.

LC-MS of intracellular metabolites. LC-MS analysis was carried out as described previously (27, 80). Chromatographic separation occurred on a 2.1- by 100-mm Acquity ultrahigh-pressure liquid chromatography ethylene bridged hybrid (UHPLC BEH) C_{18} column with 1.7-μm particle size (Waters) at 25°C on a Vanquish UPLC coupled to a Q Exactive Orbitrap high-resolution mass spectrometer (ThermoScientific) using an electrospray ionization source operating in negative mode. Intracellular metabolites were dried out of extraction solvent using N_2 and resuspended in solvent A (97:3 H_2O-methanol with 10 mM tributylamine adjusted to pH 8.2 by the addition of acetic acid to ~10 mM final concentration). Solvent B was 100% methanol. Separation was achieved using the following gradient: 0 to 2.5 min, 5% B; 2.5 to 17 min, linear gradient from 5% B to 95% B; 17 to 19.5 min, 95% B; 19.5 to 20 min, linear gradient from 95% B to 5% B; 20 to 25 min, 5% B. Mass spectrometry parameters were full MS-SIM (single-ion monitoring) scanning between 70 and 1,000 m/z, automatic control gain (ACG) target of 1e6, maximum injection time (IT) of 40 ms, and resolution of 70,000 or 140,000 full width at half maximum (FWHM). Compounds were identified by retention time matching to pure standards and monoisotopic mass. Data were analyzed using the MAVEN software suite (81, 82). Metabolite mass isotopomer distributions (MIDs) from ^{13}C labeling samples were corrected for ^{13}C natural abundance using ElemCor (83), and the corrected MIDs were used throughout the text and graphs (see Table S4 in the supplemental material). ^2H labeling data were not corrected for the natural abundance of ^2H (~0.02% abundance).

Intracellular metabolite quantitation. Intracellular metabolite concentrations were measured by growing *E. coli* RL3000 in medium containing solely [U-$^{13}C_6$]glucose and then extracting intracellular metabolites into solvent containing known concentrations of unlabeled standards for metabolites of interest. The solvent containing ^{13}C-labeled intracellular metabolites and unlabeled standards was analyzed by LC-MS, and the ratio between the ^{13}C and ^{12}C peak intensities was used to determine intracellular metabolite concentrations (84). *E. coli* grown with [U-$^{13}C_6$]glucose was also extracted into solvent without standards, which was mixed in 1:5, 1:1, and 5:1 proportions with extracts from either *C. thermocellum* grown on cellobiose or *T. saccharolyticum* grown on glucose. The mixed samples were analyzed by LC-MS, and the ratio between labeled and unlabeled metabolite signals, combined with the

calculated concentrations in *E. coli*, were used to measure metabolite concentrations in *C. thermocellum* and *T. saccharolyticum*. Intracellular metabolite quantitation was performed in biological triplicate.

Aniline derivatization. To enhance chromatographic separation and detection of some metabolites, we performed an aniline derivatization protocol for some samples used for metabolite quantitation (46). After the extraction of metabolites as described above, 100 μl extract was dried under N_2 and then reconstituted in water. Ten microliters N-(3-dimethylaminopropyl)-N'-ethylcarbodiimide hydrochloride (EDC) solution and 10 μl 6 M aniline solution was added. Samples were vortexed for 2 h, and then 5 μl triethylamine was added to stop the reaction. Samples were centrifuged to remove debris and then subjected to LC-MS analysis as described above.

Positional labeling in pyruvate and acetyl group labeling. Positional labeling in pyruvate was determined by comparing the labeling patterns in ornithine (Orn) with those in acetylornithine (AcOrn). These compounds differ by a single acetyl group, received from acetyl-CoA, which is itself produced by decarboxylation of pyruvate. Thus, the acetyl group always contains only the 2nd and 3rd carbons of pyruvate, and the gain of labeled carbons by Orn during acetylation to AcOrn can be used as a readout of the position of labeled carbons in pyruvate. Acetyl group labeling was also measured by comparing the labeling patterns of glucosamine-6-phosphate to those in N-acetyl-glucosamine-6-phosphate.

CO_2 labeling. During ^{13}C labeling, unlabeled CO_2 may come from two sources: (i) glucose dissimilation and (ii) carryover from inoculation. For glucose dissimulation, in cultures fed an equimolar mixture of [U$^{13}C_6$]glucose and unlabeled glucose, ~50% of CO_2 released during glucose fermentation to ethanol or acetate is expected to be unlabeled; the decarboxylation of pyruvate to form acetyl-CoA likely releases most of the cell-produced CO_2. In cultures fed [1-$^{13}C_1$]- or [6-$^{13}C_1$]glucose, almost all CO_2 released by the culture would be unlabeled. The ^{13}C carbon under these conditions becomes the methyl carbon of pyruvate (Fig. 2), leaving the carboxyl carbon released by decarboxylation unlabeled. For carryover from inoculation, cultures were inoculated from a preculture containing unlabeled carbon sources, allowing unlabeled CO_2 to be produced in the preculture and transferred to the working culture by syringe during inoculation.

To determine the labeling of intracellular CO_2, we compared the labeling patterns of Orn with those of citrulline (Citr), which differs from Orn by incorporation of a single CO_2 molecule. Thus, the difference between the labeling patterns of the two metabolites is due to the labeling of CO_2. We used CO_2 labeling derived this way solely to assist in our qualitative analysis of metabolism; CO_2 was not assigned an MID during MFA.

THF intermediate and mock purine labeling. THF intermediate labeling was measured by comparing the labeling patterns of threonine (Thr) to the labeling pattern of methionine (Met). Met is formed from threonine by the addition of a single carbon from 5-methyltetrahydrofolate (MTHF), derived from the same pool as FTHF. Thus, the difference between Thr and Met labeling allowed us to determine FTHF labeling. Labeling of "mock purine" was produced by combining the labeling patterns of all precursors to purine formation, ribose-5-phosphate (R5P), glycine (gly), 2 THF intermediates, and CO_2, into a single hypothetical MID for purines. This simulated MID showed agreement with measured labeling of purines ATP and GTP (Fig. S3C).

Metabolic network model construction. The *T. saccharolyticum* metabolic model was constructed from the KEGG genome-scale metabolic model, manually curated (10, 12, 22, 23) (Table S5A). The model contains the major central metabolic reactions from the EMP, nonoxidative pentose phosphate, and TCA pathways, along with fermentative, amino acid biosynthetic, and biomass-forming reactions. We constructed models containing alternative versions of pathways (i.e., an Entner-Doudoroff glycolytic pathway in addition to or instead of EMP glycolysis, a complete oxidative TCA cycle, or an oxidative PPP) to confirm that these pathways lacked activity in *T. saccharolyticum*. Our largest additions to the final genome-scale model were the inclusion of a complete set of reactions producing serine from 3-phosphoglycerate, gap filling of the citramalate pathway for isoleucine biosynthesis, and addition of an SBP bypass for the PPP, all of which were supported by qualitative analysis of steady-state labeling experiments and better model fits.

The *C. thermocellum* metabolic model was constructed using published metabolic network reconstructions, combined with KEGG annotations and manual curation (12, 18, 20–24, 26) (Table S5B). The model contains the major central metabolic reactions from the EMP, nonoxidative pentose phosphate, and TCA pathways, along with fermentative, amino acid biosynthetic, and biomass-forming reactions.

Metabolic flux analysis. MFA was performed using the INCA software suite (63). INCA is implemented in Matlab and simulates isotopic distributions according to the elementary metabolite unit (EMU) framework (64). We estimated intracellular fluxes by solving a nonlinear least-squares regression problem that minimizes the variance-weighted sum of squared residuals (SSR) between simulated and measured isotopic distributions of intracellular and extracellular metabolites. We combined all tracer data sets, together with uptake, excretion, and growth rates, for each organism into a single, statistically acceptable flux map using the COMPLETE-MFA technique (85). Labeling data from ^{13}C and ^2H tracer experiments were entered into INCA without correction for naturally abundant heavy isotopes (Table S6). We restarted flux estimation 25 times using random initial parameters to ensure a global SSR minimum had been reached. Reversible reactions were modeled as a forward and backward reaction. Net fluxes (J_{net}) equals forward flux (J^+) minus backward flux (J^-), and exchange flux (J_{exch}) equals min(J^+, J^-). Using the optimal solution, we calculated 95% confidence intervals for all estimated fluxes by performing a parameter continuation, which varies each flux to determine how sensitive the optimal SSR is to that flux. Upper and lower bounds are assigned to each flux by finding how far they can be varied before the SSR is perturbed past a critical point, corresponding to a chi-square distribution with a single degree of freedom.

Some metabolites, such as pyruvate, malate, and fumarate, were present in both the cytosol and fermentation broth but did not appear to be taken up and used by the cell, just excreted over time. To account for the extracellular fractions of these metabolites, we modeled them in such a way as to allow dilution with their naturally labeled equivalents without allowing other reactions to access the naturally labeled fractions of these metabolites. Dilution is also present due to the incorporation of unlabeled atmospheric CO_2, which was modeled by allowing intracellular CO_2 to exchange with a pool of unlabeled CO_2. We used a previously published biomass equation (86) and ethanol excretion rate (26), together with our measured uptake and excretion fluxes for lactate, acetate, glucose, and formate in *C. thermocellum*. The remaining glucose consumption was assigned to pyruvate, valine, asparagine, and alanine proportional to previous reported amounts (87).

Measured uptake and excretion fluxes for biomass, lactate, ethanol, acetate, and glucose in *T. saccharolyticum* were assigned based on previously reported end product titers (10, 39). Our analysis was unable to fully resolve the contributions of Ppdk versus the malate shunt regarding PEP-to-pyruvate flux. We therefore constructed two versions of the *C. thermocellum* model, whose only difference was the inclusion or omission of malic enzyme, and compared glycolytic flux ratios (J^+/J^-) and the derived free energies across them. We found a <1.0% cumulative difference in free energy of glycolytic reactions between the two models, with the single most affected reaction having only a 5.5% difference in free energy. Thus, the omission of malic enzyme had a negligible effect on ΔG measurements, and this model was used for all flux and free energy calculations presented in the text and figures.

Goodness-of-fit analysis. A χ^2 test was used to determine whether the estimated fluxes adequately describe the measured data. The optimized SSR of a correct model and data set is a variable with a χ^2 distribution with degrees of freedom equal to the number of fitted measurements (n) minus the number of estimated independent parameters (p). Fitted measurements are fitted external fluxes, namely, uptake, excretion, growth rates, and all non-zero MIDs. Estimated parameters are all free fluxes, including net, exchange, and dilution fluxes. We required that our models pass the χ^2 test with a critical threshold of 0.05 (95% confidence), meaning the optimized SSR fell between $\chi^2_{\alpha/2}(n - p)$ and $\chi^2_{1-\alpha/2}(n - p)$. For *C. thermocellum*, the acceptable SSR range was 422.1 to 543.7, and the SSR after convergence was 499.2. For *T. saccharolyticum*, the acceptable SSR range was 434.3 to 557.5, and the SSR after convergence was 507.3.

Estimation of Gibbs free energies. Reaction free energies were calculated from MFA-derived flux measurements using the relation $\Delta G = -RT \ln(J^+/J^-)$. For two reactions (Pfk and Pyk) in the glycolytic pathway of *T. saccharolyticum*, the 95% confidence interval lower bound for the reverse flux was 0, implying the reaction free energy is unbounded in the negative direction (i.e., the free energy is determined to be less than a discrete value with no lower bound). For these reactions, we supplemented our flux-based ΔG values with those calculated from metabolite concentrations using the relation $\Delta G = \Delta G^{\circ\prime} + RT \ln Q$, where Q is the ratio of the concentrations of products to reactants, R is the gas constant, and T is temperature in kelvin. Reaction standard free energies ($\Delta G^{\circ\prime}$) were retrieved from the online tool eQuilibrator, using a pH of 7 and ionic strength of 0.1 as settings (50, 88, 89). Metabolite concentrations provided a tighter bound on reaction free energies. The published reaction free energies for anaerobically grown *E. coli* (29) combine Pgi and Pfk as a single lumped reaction (Pgi-Pfk), so we supplemented these values with the free energy of Pgi and Pfk calculated from our measured intracellular metabolite concentrations for display (Fig. S4).

SUPPLEMENTAL MATERIAL

Supplemental material is available online only.

FIG S1, PDF file, 0.6 MB.
FIG S2, PDF file, 0.6 MB.
FIG S3, PDF file, 0.7 MB.
FIG S4, PDF file, 0.4 MB.
TABLE S1, XLSX file, 0.01 MB.
TABLE S2, XLSX file, 0.03 MB.
TABLE S3, XLSX file, 0.01 MB.
TABLE S4, XLSX file, 0.1 MB.
TABLE S5, XLSX file, 0.02 MB.
TABLE S6, XLSX file, 0.05 MB.

REFERENCES

1. Olson DG, Mcbride JE, Shaw AJ, Lynd LR. 2012. Recent progress in consolidated bioprocessing. Curr Opin Biotechnol 23:396–405. https://doi.org/10.1016/j.copbio.2011.11.026.

2. Yee KL, Rodriguez M, Thompson OA, Fu C, Wang Z-Y, Davison BH, Mielenz JR. 2014. Consolidated bioprocessing of transgenic switchgrass by an engineered and evolved *Clostridium thermocellum* strain. Biotechnol Biofuels 7:75. https://doi.org/10.1186/1754-6834-7-75.

3. Herring CD, Kenealy WR, Joe Shaw A, Covalla SF, Olson DG, Zhang J, Ryan Sillers W, Tsakraklides V, Bardsley JS, Rogers SR, Thorne PG, Johnson JP, Foster A, Shikhare ID, Klingeman DM, Brown SD, Davison BH, Lynd LR, Hogsett DA. 2016. Strain and bioprocess improvement of a thermophilic anaerobe for the production of ethanol from wood. Biotechnol Biofuels 9:125. https://doi.org/10.1186/s13068-016-0536-8.

4. Lee Y-E, Jain MK, Lee C, Lowe SE, Zeikus JG. 1993. Taxonomic distinction of saccharolytic thermophilic anaerobes: description of *Thermoanaerobacterium xylanolyticum* gen. nov., sp. nov., and *Thermoanaerobacterium saccharolyticum* gen. nov., sp. nov.; reclassification of *Thermoanaerobium brockii*, *Clostridium thermosulfurogenes*, and *Clostridium thermohydrosulfuricum* E100-69 as *Thermoanaerobacter brockii* comb. nov., *Thermoanaerobacterium thermosulfurigenes* comb. nov., and *Thermoanaerobacter thermohydrosulfuricus* comb. nov., respectively; and transfer of *Clostridium thermohydrosulfuricum* 39E to *Thermoanaerobacter ethanolicus*. Int J Syst Bacteriol 43:41–51. https://doi.org/10.1099/00207713-43-1-41.

5. Demain AL, Newcomb M, Wu JHD, Demain AL, Newcomb M, Wu J. 2005. Cellulase, Clostridia, and ethanol. Microbiol Mol Biol Rev 69:124–154. https://doi.org/10.1128/MMBR.69.1.124-154.2005.

6. Tian L, Papanek B, Olson DG, Rydzak T, Holwerda EK, Zheng T, Zhou J, Maloney M, Jiang N, Giannone R, Hettich R, Guss A, Lynd L. 2016. Simultaneous achievement of high ethanol yield and titer in Clostridium thermocellum. Biotechnol Biofuels 9:1–11. https://doi.org/10.1186/s13068-016-0528-8.

7. Yang S, Fei Q, Zhang Y, Contreras LM, Utturkar SM, Steven D, Himmel ME, Zhang M. 2016. *Zymomonas mobilis* as a model system for production of biofuels and biochemicals. Microb Biotechnol 9:699–717. https://doi.org/10.1111/1751-7915.12408.

8. Nielsen J, Larsson C, van Maris A, Pronk J. 2013. Metabolic engineering of yeast for production of fuels and chemicals. Curr Opin Biotechnol 24:398–404. https://doi.org/10.1016/j.copbio.2013.03.023.

9. Lau MW, Gunawan C, Balan V, Dale BE. 2010. Comparing the fermentation performance of *Escherichia coli* KO11, *Saccharomyces cerevisiae* 424A(LNH-ST) and *Zymomonas mobilis* AX101 for cellulosic ethanol production. Biotechnol Biofuels 3:11. https://doi.org/10.1186/1754-6834-3-11.

10. Shaw AJ, Podkaminer KK, Desai SG, Bardsley JS, Rogers SR, Thorne PG, Hogsett DA, Lynd LR. 2008. Metabolic engineering of a thermophilic bacterium to produce ethanol at high yield. Proc Natl Acad Sci U S A 105:13769–13774. https://doi.org/10.1073/pnas.0801266105.

11. Argyros DA, Tripathi SA, Barrett TF, Rogers SR, Feinberg LF, Olson DG, Foden JM, Miller BB, Lynd LR, Hogsett DA, Caiazza NC. 2011. High ethanol titers from cellulose by using metabolically engineered thermophilic, anaerobic microbes. Appl Environ Microbiol 77:8288–8294. https://doi.org/10.1128/AEM.00646-11.

12. Cui J, Olson DG, Lynd LR. 2019. Characterization of the *Clostridium thermocellum* AdhE, NfnAB, ferredoxin and Pfor proteins for their ability to support high titer ethanol production in *Thermoanaerobacterium saccharolyticum*. Metab Eng 51:32–42. https://doi.org/10.1016/j.ymben.2018.09.006.

13. Deng Y, Olson DG, Zhou J, Herring CD, Joe Shaw A, Lynd LR. 2013. Redirecting carbon flux through exogenous pyruvate kinase to achieve high ethanol yields in *Clostridium thermocellum*. Metab Eng 15:151–158. https://doi.org/10.1016/j.ymben.2012.11.006.

14. Tian L, Perot SJ, Stevenson D, Jacobson TB, Lanahan AA, Amador-Noguez D, Olson DG, Lynd LR. 2017. Metabolome analysis reveals a role for glyceraldehyde 3–phosphate dehydrogenase in the inhibition of *C. thermocellum* by ethanol. Biotechnol Biofuels 10:276. https://doi.org/10.1186/s13068-017-0961-3.

15. Zheng T, Olson DG, Tian L, Bomble YJ, Himmel ME, Lo J, Hon S, Shaw AJ, van Dijken JP, Lynd LR. 2015. Cofactor specificity of the bifunctional alcohol and aldehyde dehydrogenase (AdhE) in wild-type and mutant *Clostridium thermocellum* and *Thermoanaerobacterium saccharolyticum*. J Bacteriol 197:2610–2619. https://doi.org/10.1128/JB.00232-15.

16. Hon S, Olson DG, Holwerda EK, Lanahan AA, Murphy SJL, Maloney MI, Zheng T, Papanek B, Guss AM, Lynd LR. 2017. The ethanol pathway from *Thermoanaerobacterium saccharolyticum* improves ethanol production in *Clostridium thermocellum*. Metab Eng 42:175–184. https://doi.org/10.1016/j.ymben.2017.06.011.

17. Tian L, Lo J, Shao X, Zheng T, Olson DG, Lynd LR. 2016. Ferredoxin:NAD+ oxidoreductase of *Thermoanaerobacterium saccharolyticum* and its role in ethanol formation. Appl Environ Microbiol 82:7134–7141. https://doi.org/10.1128/AEM.02130-16.

18. Olson DG, Hörl M, Fuhrer T, Cui J, Zhou J, Maloney IM, Amador-Noguez D, Tian L, Sauer U, Lynd LR. 2017. Glycolysis without pyruvate kinase in *Clostridium thermocellum*. Metab Eng 39:169–180. https://doi.org/10.1016/j.ymben.2016.11.011.

19. Lynd LR, Guss AM, Himmel ME, Beri D, Herring C, Holwerda EK, Murphy SJ, Olson DG, Paye J, Rydzak T, Shao X, Tian L, Worthen R. 2017. Advances in consolidated bioprocessing using *Clostridium thermocellum* and *Thermoanaerobacter saccharolyticum*, p 365–394. *In* Wittmann C, Liao JC (ed), Industrial biotechnology. Wiley-VHC, New York, NY.

20. Zhou J, Olson DG, Argyros DA, Deng Y, van Gulik WM, van Dijken JP, Lynd LR. 2013. Atypical glycolysis in *Clostridium thermocellum*. Appl Environ Microbiol 79:3000–3008. https://doi.org/10.1128/AEM.04037-12.

21. Taillefer M, Rydzak T, Levin DB, Oresnik IJ, Sparling R. 2015. Reassessment of the transhydrogenase/malate shunt pathway in *Clostridium thermocellum* ATCC 27405 through kinetic characterization of malic enzyme and malate dehydrogenase. Appl Environ Microbiol 81:2423–2432. https://doi.org/10.1128/AEM.03360-14.

22. Kanehisa M, Goto S. 2000. KEGG: Kyoto encyclopaedia of genes and genomes. Nucleic Acids Res 28:27–30. https://doi.org/10.1093/nar/28.1.27.

23. Kanehisa M, Sato Y, Furumichi M, Morishima K, Tanabe M. 2019. New approach for understanding genome variations in KEGG. Nucleic Acids Res 47:590–595.

24. Rydzak T, McQueen PD, Krokhin OV, Spicer V, Ezzati P, Dwivedi RC, Shamshurin D, Levin DB, Wilkins JA, Sparling R. 2012. Proteomic analysis of Clostridium thermocellum core metabolism: relative protein expression profiles and growth phase-dependent changes in protein expression. BMC Microbiol 12:214–218. https://doi.org/10.1186/1471-2180-12-214.

25. Mertens E. 1991. Pyrophosphate-dependent phosphofructokinase, an anaerobic glycolytic enzyme? FEBS J 285:1–5. https://doi.org/10.1016/0014-5793(91)80711-B.

26. Xiong W, Lo J, Chou KJ, Wu C, Magnusson L, Dong T, Maness P. 2018. Isotope-assisted metabolite analysis sheds light on central carbon metabolism of a model cellulolytic bacterium *Clostridium thermocellum*. Front Microbiol 9:1–11. https://doi.org/10.3389/fmicb.2018.01947.

27. Jacobson TB, Adamczyk PA, Stevenson DM, Regner M, Ralph J, Reed JL, Amador-Noguez D. 2019. ^{2}H and ^{13}C metabolic flux analysis elucidates in vivo thermodynamics of the ED pathway in *Zymomonas mobilis*. Metab Eng 54:301–316. https://doi.org/10.1016/j.ymben.2019.05.006.

28. Park JO, Rubin SA, Xu YF, Amador-Noguez D, Fan J, Shlomi T, Rabinowitz JD. 2016. Metabolite concentrations, fluxes, and free energies imply efficient enzyme usage. Nat Chem Biol 12:482–489. https://doi.org/10.1038/nchembio.2077.

29. Park JO, Tanner LB, Wei MH, Khana DB, Jacobson TB, Zhang Z, Rubin SA, Li S-J, Higgins MB, Stevenson DM, Amador-Noguez D, Rabinowitz JD. 2019. Near-equilibrium glycolysis supports metabolic homeostasis and energy yield. Nat Chem Biol 15:1001–1008. https://doi.org/10.1038/s41589-019-0364-9.

30. Beard DA, Qian H. 2007. Relationship between thermodynamic driving force and one-way fluxes in reversible processes. PLoS One 2:e144–e146. https://doi.org/10.1371/journal.pone.0000144.

31. Flamholz A, Noor E, Bar-Even A, Liebermeister W, Milo R. 2013. Glycolytic strategy as a tradeoff between energy yield and protein cost. Proc Natl Acad Sci U S A 110:10039–10044. https://doi.org/10.1073/pnas.1215283110.

32. Noor E, Bar-Even A, Flamholz A, Reznik E, Liebermeister W, Milo R. 2014. Pathway thermodynamics highlights kinetic obstacles in central metabolism. PLoS Comput Biol 10:e1003483-12. https://doi.org/10.1371/journal.pcbi.1003483.

33. Noor E, Flamholz A, Bar-Even A, Davidi D, Milo R, Liebermeister W. 2016. The protein cost of metabolic fluxes: prediction from enzymatic rate laws and cost minimization. PLoS Comput Biol 12:e1005167. https://doi.org/10.1371/journal.pcbi.1005167.

34. Tepper N, Noor E, Amador-Noguez D, Haraldsdóttir HS, Milo R, Rabinowitz J, Liebermeister W, Shlomi T. 2013. Steady-state metabolite concentrations reflect a balance between maximizing enzyme efficiency and

minimizing total metabolite load. PLoS One 8:e75370-13. https://doi.org/10.1371/journal.pone.0075370.

35. Lamed R, Zeikus JG. 1980. Ethanol production by thermophilic bacteria: relationship between fermentation product yields of and catabolic enzyme activities in *Clostridium thermocellum* and *Thermoanaerobium brockii*. J Bacteriol 144:569–578. https://doi.org/10.1128/JB.144.2.569-578.1980.

36. Williams TI, Combs JC, Lynn BC, Strobel HJ. 2007. Proteomic profile changes in membranes of ethanol-tolerant *Clostridium thermocellum*. Appl Microbiol Biotechnol 74:422–432. https://doi.org/10.1007/s00253-006-0689-7.

37. Raman B, McKeown CK, Rodriguez M, Jr, Brown SD, Mielenz JR. 2011. Transcriptomic analysis of *Clostridium thermocellum* ATCC 27405 cellulose fermentation. BMC Microbiol 11:134–115. https://doi.org/10.1186/1471-2180-11-134.

38. Holwerda EK, Thorne PG, Olson DG, Amador-Noguez D, Engle NL, Tschaplinski TJ, van Dijken JP, Lynd LR. 2014. The exometabolome of *Clostridium thermocellum* reveals overflow metabolism at high cellulose loading. Biotechnol Biofuels 7:155. https://doi.org/10.1186/s13068-014-0155-1.

39. Currie DH, Raman B, Gowen CM, Tschaplinski TJ, Land ML, Brown SD, Covalla SF, Klingeman DM, Yang ZK, Engle NL, Johnson CM, Rodriguez M, Shaw AJ, Kenealy WR, Lynd LR, Fong SS, Mielenz JR, Davison BH, Hogsett DA, Herring CD. 2015. Genome-scale resources for *Thermoanaerobacterium saccharolyticum*. BMC Syst Biol 9:1–15. https://doi.org/10.1186/s12918-015-0159-x.

40. Currie DH, Guss AM, Herring CD, Giannone RJ, Johnson CM, Lankford PK, Brown SD, Hettich RL, Lynd LR. 2014. Profile of secreted hydrolases, associated proteins, and SlpA in *Thermoanaerobacterium saccharolyticum* during the degradation of hemicellulose. Appl Environ Microbiol 80:5001–5011. https://doi.org/10.1128/AEM.00998-14.

41. Romano AH, Conway T. 1996. Evolution of carbohydrate metabolic pathways. Res Microbiol 147:448–455. https://doi.org/10.1016/0923-2508(96)83998-2.

42. Xavier KB, Da Costa MS, Santos H. 2000. Demonstration of a novel glycolytic pathway in the hyperthermophilic archaeon *Thermococcus zilligii* by ¹³C-labeling experiments and nuclear magnetic resonance analysis. J Bacteriol 182:4632–4636. https://doi.org/10.1128/jb.182.16.4632-4636.2000.

43. Hackmann TJ, Ngugi DK, Firkins JL, Tao J. 2017. Genomes of rumen bacteria encode atypical pathways for fermenting hexoses to short-chain fatty acids. Environ Microbiol 19:4670–4683. https://doi.org/10.1111/1462-2920.13929.

44. Fuhrman LK, Wanken A, Nickerson KW, Conway T. 1998. Rapid accumulation of intracellular 2-keto-3-deoxy-6-phosphogluconate in an Entner-Doudoroff aldolase mutant results in bacteriostasis. FEMS Microbiol Lett 159:261–266. https://doi.org/10.1111/j.1574-6968.1998.tb12870.x.

45. The UniProt Consortium. 2019. UniProt: a worldwide hub of protein knowledge. Nucleic Acids Res 47:506–515. https://doi.org/10.1093/nar/gky1049.

46. Yang W-C, Sedlak M, Regnier FE, Mosier N, Ho N, Adamec J. 2008. Simultaneous quantification of metabolites involved in central carbon and energy metabolism using reversed-phase liquid chromatography-mass spectrometry and in vitro ¹³C labeling. Anal Chem 80:9508–9516. https://doi.org/10.1021/ac801693c.

47. Bennett BD, Kimball EH, Gao M, Osterhout R, Van Dien SJ, Rabinowitz JD. 2009. Absolute metabolite concentrations and implied enzyme active site occupancy in *Escherichia coli*. Nat Chem Biol 5:593–599. https://doi.org/10.1038/nchembio.186.

48. Clasquin MF, Melamud E, Singer A, Gooding JR, Xu X, Dong A, Cui H, Campagna SR, Savchenko A, Yakunin AF, Rabinowitz JD, Caudy AA. 2011. Riboneogenesis in yeast. Cell 145:969–980. https://doi.org/10.1016/j.cell.2011.05.022.

49. Risso C, Van Dien SJ, Orloff A, Lovley DR, Coppi MV. 2008. Elucidation of an alternate isoleucine biosynthesis pathway in *Geobacter sulfurreducens*. J Bacteriol 190:2266–2274. https://doi.org/10.1128/JB.01841-07.

50. Flamholz A, Noor E, Bar-Even A, Milo R. 2012. eQuilibrator—the biochemical thermodynamics calculator. Nucleic Acids Res 40:770–775. https://doi.org/10.1093/nar/gkr874.

51. Zhou J. 2016. Comparative analysis of central metabolism in three thermophilic saccharolytic bacteria. Dissertation. Thayer School of Engineering, Dartmouth College, Hannover, NH.

52. Escalante A, Cervantes AS, Gosset G, Bolívar F. 2012. Current knowledge of the *Escherichia coli* phosphoenolpyruvate–carbohydrate phospho-

transferase system: peculiarities of regulation and impact on growth and product formation. Appl Microbiol Biotechnol 94:1483–1494. https://doi.org/10.1007/s00253-012-4101-5.

53. Tsakraklides V, Shaw AJ, Miller BB, Hogsett DA, Herring CD. 2012. Carbon catabolite repression in *Thermoanaerobacterium saccharolyticum*. Biotechnol Biofuels 5:85. https://doi.org/10.1186/1754-6834-5-85.

54. Rydzak T, Grigoryan M, Cunningham ZJ, Krokhin OV, Ezzati P, Cicek N, Levin DB, Wilkins JA, Sparling R. 2014. Insights into electron flux through manipulation of fermentation conditions and assessment of protein expression profiles in *Clostridium thermocellum*. Appl Microbiol Biotechnol 98:6497–6510. https://doi.org/10.1007/s00253-014-5798-0.

55. Rydzak T, Lynd LR, Guss AM. 2015. Elimination of formate production in *Clostridium thermocellum*. J Ind Microbiol Biotechnol 42:1263–1272. https://doi.org/10.1007/s10295-015-1644-3.

56. Rydzak T, Levin DB, Cicek N, Sparling R. 2011. End-product induced metabolic shifts in *Clostridium thermocellum* ATCC 27405. Appl Microbiol Biotechnol 92:199–209. https://doi.org/10.1007/s00253-011-3511-0.

57. Zhou J, Olson DG, Lanahan AA, Tian L, Murphy S-L, Lo J, Lynd LR. 2015. Physiological roles of pyruvate ferredoxin oxidoreductase and pyruvate formate-lyase in *Thermoanaerobacterium saccharolyticum* JW/SL-YS485. Biotechnol Biofuels 8:1–14. https://doi.org/10.1186/s13068-015-0304-1.

58. Dietrich J, Henning U. 1970. Regulation of pyruvate dehydrogenase complex synthesis. Eur J Biochem 14:258–269. https://doi.org/10.1111/j.1432-1033.1970.tb00285.x.

59. Knappe J, Schacht J, Möckel W, Höpner T, Vetter H, Edenharder R. 1969. Pyruvate formate-lyase reaction in *Escherichia coli*. Eur J Biochem 11:316–327. https://doi.org/10.1111/j.1432-1033.1969.tb00775.x.

60. Amador-Noguez D, Feng X-J, Fan J, Roquet N, Rabitz H, Rabinowitz JD. 2010. Systems-level metabolic flux profiling elucidates a complete, bifurcated tricarboxylic acid cycle in *Clostridium acetobutylicum*. J Bacteriol 192:4452–4461. https://doi.org/10.1128/JB.00490-10.

61. Mall A, Sobotta J, Huber C, Tschirner C, Kowarschik S, Bacnik K, Mergelsberg M, Boll M, Hügler M, Eisenreich W, Berg IA. 2018. Reversibility of citrate synthase allows autotrophic growth of a thermophilic bacterium. Science 567:563–567. https://doi.org/10.1126/science.aao2410.

62. Nunoura T, Chikaraishi Y, Izaki R, Suwa T, Sato T, Harada T, Mori K, Kato Y, Miyazaki M, Shimamura S, Yanagawa K, Shuto A, Ohkouchi N, Fujita N, Takaki Y, Atomi H, Takai K. 2018. A primordial and reversible TCA cycle in a facultatively chemolithoautotrophic thermophile. Science 563:559–563. https://doi.org/10.1126/science.aao3407.

63. Young JD. 2014. INCA : a computational platform for isotopically nonstationary metabolic flux analysis. Bioinformatics 30:1333–1335. https://doi.org/10.1093/bioinformatics/btu015.

64. Antoniewicz MR, Kelleher JK, Stephanopoulos G. 2007. Elementary metabolite units (EMU): a novel framework for modeling isotopic distributions. Metab Eng 9:68–86. https://doi.org/10.1016/j.ymben.2006.09.001.

65. Bar-Even A, Flamholz A, Noor E, Milo R. 2012. Rethinking glycolysis: on the biochemical logic of metabolic pathways. Nat Chem Biol 8:509–517. https://doi.org/10.1038/nchembio.971.

66. Dekel E, Alon U. 2005. Optimality and evolutionary tuning of the expression level of a protein. Nat Lett 436:588–592. https://doi.org/10.1038/nature03842.

67. Zhang L, Tang Y, Guo Z, Ding Z, Shi G. 2011. Improving the ethanol yield by reducing glycerol formation using cofactor regulation in *Saccharomyces cerevisiae*. Biotechnol Lett 33:1375–1380. https://doi.org/10.1007/s10529-011-0588-6.

68. Chen X, Kuhn E, Jennings EW, Nelson R, Tao L, Zhang M, Tucker MP. 2016. DMR (deacetylation and mechanical refining) processing of corn stover achieves high monomeric sugar concentrations (230 g L⁻¹) during enzymatic hydrolysis and high ethanol concentrations (>10% v/v) during fermentation without hydrolysate purification or concentration. Energy Environ Sci 9:1237–1245. https://doi.org/10.1039/C5EE03718B.

69. Wang H, Cao S, Wang WT, Wang KT, Jia X. 2016. Very high gravity ethanol and fatty acid production of *Zymomonas mobilis* without amino acid and vitamin. J Ind Microbiol Biotechnol 43:861–871. https://doi.org/10.1007/s10295-016-1761-7.

70. Dash S, Olson DG, Chan SHJ, Amador-Noguez D, Lynd LR, Maranas CD. 2019. Thermodynamic analysis of the pathway for ethanol production from cellobiose in *Clostridium thermocellum*. Metab Eng 55:161–169. https://doi.org/10.1016/j.ymben.2019.06.006.

71. Li Y, Tschaplinski TJ, Engle NL, Hamilton CY, Rodriguez M, Jr, Liao JC, Schadt CW, Guss AM, Yang Y, Graham DE. 2012. Combined inactivation of the *Clostridium cellulolyticum* lactate and malate dehydrogenase genes substantially increases ethanol yield from cellulose and switch-

grass fermentations. Biotechnol Biofuels 5:2. https://doi.org/10.1186/1754-6834-5-2.

72. Koebmann BJ, Westerhoff HV, Snoep JL, Nilsson D, Jensen PR. 2002. The glycolytic flux in *Escherichia coli* is controlled by the demand for ATP. J Bacteriol 184:3909–3916. https://doi.org/10.1128/jb.184.14.3909-3916.2002.

73. Larsson C, Nilsson A, Blomberg A, Gustafsson L. 1997. Glycolytic flux is conditionally correlated with ATP concentration in *Saccharomyces cerevisiae*: a chemostat study under carbon- or nitrogen-limiting conditions. J Bacteriol 179:7243–7250. https://doi.org/10.1128/jb.179.23.7243-7250.1997.

74. Rutkis R, Kalnenieks U, Stalidzans E, Fell DA. 2013. Kinetic modelling of the *Zymomonas mobilis* Entner-Doudoroff pathway: insights into control and functionality. Microbiology 159:2674–2689. https://doi.org/10.1099/mic.0.071340-0.

75. Carere CR, Rydzak T, Verbeke TJ, Cicek N, Levin DB, Sparling R. 2012. Linking genome content to biofuel production yields: a meta-analysis of major catabolic pathways among select H_2 and ethanol-producing bacteria. BMC Microbiol 12:295. https://doi.org/10.1186/1471-2180-12-295.

76. Buckel W, Thauer RK. 2013. Energy conservation via electron bifurcating ferredoxin reduction and proton/Na^+ translocating ferredoxin oxidation. Biochim Biophys Acta 1827:94–113. https://doi.org/10.1016/j.bbabio.2012.07.002.

77. Lo J, Olson DG, Murphy S-L, Tian L, Hon S, Lanahan A, Guss AM, Lynd LR. 2017. Engineering electron metabolism to increase ethanol production in *Clostridium thermocellum*. Metab Eng 39:71–79. https://doi.org/10.1016/j.ymben.2016.10.018.

78. Sprenger GA. 1996. Carbohydrate metabolism in Zymomonas mobilis: a catabolic highway with some scenic routes. FEMS Microbiol Lett 145:301–307. https://doi.org/10.1111/j.1574-6968.1996.tb08593.x.

79. Ghosh IN, Landick R. 2016. OptSSeq: high-throughput sequencing readout of growth enrichment defines optimal gene expression elements for homoethanologenesis. ACS Synth Biol 5:1519–1534. https://doi.org/10.1021/acssynbio.6b00121.

80. Pisithkul T, Jacobson TB, O'Brien TJ, Stevenson DM, Amador-Noguez D. 2015. Phenolic amides are potent inhibitors of *de novo* nucleotide

biosynthesis. Appl Environ Microbiol 81:5761–5772. https://doi.org/10.1128/AEM.01324-15.

81. Clasquin MF, Melamud E, Rabinowitz JD. 2012. LC-MS data processing with MAVEN: a metabolomic analysis and visualization engine. Curr Protoc Bioinforma Chapter 14:Unit14.11. https://doi.org/10.1002/0471250953.bi1411s37.

82. Melamud E, Vastag L, Rabinowitz JD. 2010. Metabolomic analysis and visualization engine for LC-MS data. Anal Chem 82:9818–9826. https://doi.org/10.1021/ac1021166.

83. Du D, Tan L, Wang Y, Peng B, Weinstein JN, Wondisford FE, Su X, Lorenzi PL. 2019. ElemCor: accurate data analysis and enrichment calculation for high-resolution LC-MS stable isotope labeling experiments. BMC Bioinformatics 20:1–9. https://doi.org/10.1186/s12859-019-2669-9.

84. Bennett BD, Yuan J, Kimball EH, Rabinowitz JD. 2008. Absolute quantitation of intracellular metabolite concentrations by an isotope ratio-based approach. Nat Protoc 3:1299–1311. https://doi.org/10.1038/nprot.2008.107.

85. Leighty RW, Antoniewicz MR. 2013. COMPLETE-MFA: complementary parallel labeling experiments technique for metabolic flux analysis. Metab Eng 20:49–55. https://doi.org/10.1016/j.ymben.2013.08.006.

86. Dash S, Khodayari A, Zhou J, Holwerda EK, Olson DG, Lynd LR, Maranas CD. 2017. Development of a core *Clostridium thermocellum* kinetic metabolic model consistent with multiple genetic perturbations. Biotechnol Biofuels 10:1–16. https://doi.org/10.1186/s13068-017-0792-2.

87. Rydzak T, Garcia D, Stevenson DM, Sladek M, Klingeman DM, Holwerda EK, Amador-Noguez D, Brown SD, Guss AM. 2017. Deletion of type I glutamine synthetase deregulates nitrogen metabolism and increases ethanol production in *Clostridium thermocellum*. Metab Eng 41:182–191. https://doi.org/10.1016/j.ymben.2017.04.002.

88. Noor E, Bar-Even A, Flamholz A, Lubling Y, Davidi D, Milo R. 2012. An integrated open framework for thermodynamics of reactions that combines accuracy and coverage. Bioinformatics 28:2037–2044. https://doi.org/10.1093/bioinformatics/bts317.

89. Noor E, Haraldsdóttir HS, Milo R, Fleming R. 2013. Consistent estimation of Gibbs energy using component contributions. PLoS Comput Biol 9:e1003098-11. https://doi.org/10.1371/journal.pcbi.1003098.